

THESIS FOR THE DEGREE OF DOCTOR OF PHILOSOPHY

**Structure and Dynamics in Transition Metal Perovskites**  
**An Optical Spectroscopy Study**

---

JOHAN BIELECKI



**CHALMERS**

Department of Applied Physics  
CHALMERS UNIVERSITY OF TECHNOLOGY  
Gothenburg, Sweden 2012

*Structure and Dynamics in Transition Metal Perovskites*  
*An Optical Spectroscopy Study*  
JOHAN BIELECKI  
ISBN: 978-91-7385-795-6

© JOHAN BIELECKI, 2012

Doktorsavhandlingar vid Chalmers tekniska högskola  
Ny serie, nummer 3476  
ISSN 0346-718X

Department of Applied Physics  
Chalmers University of Technology  
SE-412 96 Göteborg  
Sweden  
Telephone +46 (0)31-772 1000

Chalmers Reproservice  
Göteborg, Sweden 2012

# Structure and Dynamics in Transition Metal Perovskites

## An Optical Spectroscopy Study

Johan Bielecki  
Department of Applied Physics  
Chalmers University of Technology

### Abstract

Transition metal oxides with the perovskite structure exhibit a vast number of exotic properties due to the large number of competing degrees of freedom at the Fermi surface. Together with couplings between and correlations within these degrees of freedom, this class of materials is of high interest from both a practical and theoretical point of view. In this thesis, the properties of four different perovskite systems and their relation to structure and dynamics is investigated:  $\text{La}_{1-x}\text{Ca}_x\text{MnO}_3$ , exhibiting the colossal magnetoresistance effect;  $\text{LaCoO}_3$ , undergoing spin-state transitions influenced by complicated electron-lattice interactions;  $\text{BiFeO}_3$ , one of the only known room-temperature multiferroic materials; and the proton conductor  $\text{BaInO}_3\text{H}$ .

Two kinds of optical spectroscopy methods have been used to investigate the structure and dynamics of these transition metal perovskites. Raman spectroscopy measures low-energy excitations and is, in combination with group theoretical selection rules, a sensitive probe of electronic, atomic, and magnetic structure. Ultrafast time-resolved spectroscopy is used to study, in real time, fundamental dynamics and interaction mechanisms on the femtosecond timescale.

Utilizing time resolved pump-probe reflectance spectroscopy, thermal and lattice contributions to the spin-state transition are temporarily decouple, and the first explicit observation of the high-spin repulsion in  $\text{LaCoO}_3$ , first conjectured by Goodenough in the 1950's, is presented. This opens up a novel avenue for investigating the spin-state transition in  $\text{LaCoO}_3$ . With the same experimental technique, the electron-lattice, lattice-spin, and electron-spin dynamics are investigated in  $\text{La}_{1-x}\text{Ca}_x\text{MnO}_3$ . Incorporating a two-component heat diffusion mechanism it is shown that the rate-equation based model captures all essentials of the  $>1$  ps dynamics.

Raman spectroscopy is used to investigate the structural phase-diagram of isovalently substituted  $\text{BiFeO}_3$ . The vibrational frequencies as a function of substitution provides unique input into the controversial phonon assignments of  $\text{BiFeO}_3$  and the pronounced second-order scattering is explained in terms of LO-modes activated by the Fröhlich interaction. Further, the first phonon assignment is presented and the structural transition during dehydration is investigated for  $\text{BaInO}_3\text{H}$ .

Complementing the studies on perovskites, the electron-phonon interactions are investigated in a iron-pnictide high temperature superconductor by combining Raman spectroscopy and phonon-phonon calculations. Our results point towards weak electron-phonon couplings and supports the view that a non-phononic glue is responsible for the Cooper pair condensation in iron-pnictides.

**Keywords:** *Ultrafast spectroscopy, Raman spectroscopy, magnetism, colossal magnetoresistance, multiferroics, spin-state transition, proton-conduction, high temperature superconductivity*



## List of Publications

This thesis is based on the following publications:

- I. Femtosecond optical-reflectivity measurements of lattice-mediated spin repulsions in photoexcited  $\text{LaCoO}_3$  thin-films**  
Johan Bielecki, Diana Rata and Lars Börjesson  
*Submitted to Phys. Rev. Lett.*
- II. Two Component Heat Diffusion Observed in  $\text{LaMnO}_3$  and  $\text{La}_{0.7}\text{Ca}_{0.3}\text{MnO}_3$**   
Johan Bielecki, Ralf Rauer, Ezio Zanghellini, Robert Gunnarsson, Katrin Dörr and Lars Börjesson  
*Phys. Rev. B 81, 064434 (2010)*
- III. Structural and Magnetic Properties of Isovalently Substituted Multiferroic  $\text{BiFeO}_3$ : Insights from Raman spectroscopy**  
Johan Bielecki, Peter Svedlindh, Dessie T. Tibebe, Shengzhen Cai, Sten-G. Eriksson, Lars Börjesson, and Christopher S. Knee  
*Phys. Rev. B 86, 184422 (2012)*
- IV. Local Structure and Phonon Assignment in Brownmillerite Type Oxide  $\text{Ba}_2\text{In}_2\text{O}_5$**   
Johan Bielecki, Stewart F. Parker, Dharshani Ekanayake, Lars Börjesson, and Maths Karlsson  
*In Manuscript*
- V. Local structure and hydration/dehydration properties of proton conducting brownmillerite  $\text{Ba}_2\text{In}_2\text{O}_5$  investigated with Raman Spectroscopy**  
Johan Bielecki, Stewart F. Parker, Seikh Mohammad Habibur Rahman, Christopher S. Knee, Sten-G. Eriksson, Lars Börjesson, and Maths Karlsson  
*In Manuscript*
- VI. Anharmonic softening of Raman active phonons in iron-pnictides: Estimating the Fe isotope effect due to anharmonic expansion**  
Mats Granath, Johan Bielecki, Joakim Holmlund and Lars Börjesson  
*Phys. Rev. B 79, 235103 (2009)*

## **Additional Publications not Included in the Thesis**

- VII. A statistical model of hydrogen bond networks in liquid alcohols**  
Per Sillrén, Johan Bielecki, Johan Mattsson, Lars Börjesson and Aleksandar Matic  
*Journal of Chemical Physics*, 136, 094514 (2012)
- VIII. Formation of Bone-like Nanocrystalline Apatite Using Self-Assembled Liquid Crystals**  
Wenxiao He, P. Kjellin, F. Currie, P. Handa, C. S. Knee, J. Bielecki, L. R. Wallenberg, M. Andersson  
*Chemistry of Materials*, 24, 892 (2012)
- IX. Templated Growth of Covalently Bonded Three-Dimensional Carbon Nanotube Networks Originated from Graphene**  
Yifeng Fu, Björn Carlberg, Niklas Lindahl, Niclas Lindvall, Johan Bielecki, Aleksandar Matic, Yuxin Song, Zhili Hu, Zonghe Lai, L. L. Ye, Jie Sun, Y. H. Zhang, Y. Zhang, Johan Liu  
*Advanced Materials*, 24, 1576 (2012)
- X. Selective growth of double-walled carbon nanotubes on gold films**  
Yifeng Fu, Si Chen, Johan Bielecki, Aleksandar Matic, Teng Wang, L. L. Ye, Johan Liu  
*Materials Letters*, 72, 78 (2012)
- XI. Time of Flight Mass Spectrometry to Monitor Sample Explosion in Flash Diffraction Studies on Single Virus Particles**  
Jakob Andreasson, Nicusor Timneanu, Bianca Iwan, Max Hantke, Asawari Rath, Tomas Ekeberg, Filipe R.N.C. Maia, Anton Barty, Henry N. Chapman, Johan Bielecki, Chantal Abergel, Virginie Seltzer, Jean-Michael Claverie, Martin Svenda, Daniel Rolles, Lutz Foucar, Artem Rudenko, Robert Hartmann, Christoph Bostedt and Janos Hajdu  
*In Manuscript*

# Contents

<b>1</b>	<b>Introduction</b>	<b>1</b>
<b>2</b>	<b>Structure and d-orbital Physics of Perovskites</b>	<b>3</b>
2.1	The Perovskite Structure . . . . .	3
2.2	Ligand Field Theory and Optical Transitions . . . . .	5
2.2.1	Selection Rules . . . . .	5
2.2.2	The Octahedral Energy Level Scheme . . . . .	6
2.3	The Hubbard Model . . . . .	7
2.4	Structural Effects on the Electronic and Magnetic Properties . .	9
<b>3</b>	<b>Investigated Materials</b>	<b>13</b>
3.1	Manganites . . . . .	13
3.2	BiFeO <sub>3</sub> and Multiferroicity . . . . .	16
3.3	Spin-State Transitions in LaCoO <sub>3</sub> . . . . .	20
3.4	Proton Conducting Ba <sub>2</sub> In <sub>2</sub> O <sub>5</sub> . . . . .	24
3.5	Iron-Pnictide Superconductors . . . . .	27
<b>4</b>	<b>Experimental Methods</b>	<b>33</b>
4.1	Time Resolved Spectroscopy . . . . .	33
4.1.1	Introduction to Ultrafast Optics . . . . .	34
4.1.2	Pump-Probe Spectroscopy . . . . .	39
4.1.3	Femtosecond Dynamics . . . . .	44
4.2	Raman Spectroscopy . . . . .	49
<b>5</b>	<b>Summary of Appended Papers</b>	<b>55</b>
5.1	Paper I . . . . .	55
5.2	Paper II . . . . .	56
5.3	Paper III . . . . .	57
5.4	Paper IV . . . . .	58
5.5	Paper V . . . . .	60
5.6	Paper VI . . . . .	62
	<b>Bibliography</b>	<b>65</b>



# 1

## Introduction

A large portion of the technological breakthroughs that have formed our modern society can be traced back to results obtained from fundamental research in physics, while this research is in itself based on advanced technology. This symbiotic relationship between fundamental research and technological breakthroughs is unusually fruitful in fundamental condensed matter research, where the ambition to understand materials continues to yield new applications such as for example lasers, LCD-screens, and the semiconducting materials underlying all of electronics, just to name a few.

The research frontier in condensed matter physics today is to a large extent occupied by strongly correlated materials; materials where electron-electron interactions induce correlations between electrons that are difficult to handle with the perturbative methods that have otherwise proven to be extremely useful in our understanding of matter. Part of the physicists efforts on these materials stem from pure curiosity as we do not have a fully developed conceptual framework for describing these complicated materials, but another important factor is the extreme promise they show in applications if their properties can be tamed.

Apart from the correlation between electrons, materials classed as strongly correlated often exhibit strong couplings between the electron, lattice and spin degrees of freedom, a feature that is of large interest as a basis for more efficient as well as completely new applications. This is particularly true for the variety of properties within transition metal compounds with the perovskite structure, ranging from colossal magnetoresistance[1], spin-state transitions[2], multiferroicity[3], piezoelectricity[4], proton-[5] and superconductivity[6], and catalytic behaviour[7].

In this thesis, fundamental research on a variety of transition metal based materials is presented: Perovskites in the form of manganites ( $\text{La}_{1-x}\text{Ca}_x\text{MnO}_3$ ), ferrites ( $\text{BiFeO}_3$ ), cobaltites ( $\text{LaCoO}_3$ ), and proton conductors ( $\text{BaInO}_3\text{H}$ ) together with the layered iron based superconductors ( $(\text{Nd,Ce})\text{FeAsO}_{1-x}\text{F}_x$ ).

Apart from the proton conductors, much of the exotic properties in these materials stems from strong correlations, the manifestations of which are very sensitive to internal and external parameters.

Applications based on the coupling between spins and charges, spintronics, is potentially of great use for fast and efficient storage devices, and in this context enormous efforts has been invested in the colossal magnetoresistance and electron-lattice-spin couplings in the  $\text{La}_{1-x}\text{Ca}_x\text{MnO}_3$  manganites. In the same vein, promising work has been reported on the multiferroic  $\text{BiFeO}_3$ , a material that is simultaneously ferroelectric and (anti-)ferromagnetic, which could enable completely new devices with magnetic properties modified by applying an electric field or vice versa. On the other hand, the continued strive for higher efficiency in how we use and store energy demands new materials. Here, proton conducting perovskites are possible candidates as electrolytes in intermediate-temperature fuel cells. Outside its applications in catalysis and fuel-cells, the spin-state transitions and their connection to the lattice structure in  $\text{LaCoO}_3$  has puzzled researchers for over half a century.

A different aspect of correlated electrons is superconductivity. Amongst a myriad of exotic properties found in superconductors, the most well known is the vanishing electrical resistance. The impact on applications if this low-temperature effect could be extended above room temperature would be tremendous, and so far only two classes of "high temperature" superconductors have been found: the iron-pnictides that are studied in this thesis and the cuprates.

This thesis is based on research carried out using two different types of optical spectroscopy, where the matter-photon interaction is used as a probe of dynamical and structural properties in the electronic, lattice and magnetic subsystems of the investigated materials. Time-resolved spectroscopy allows the measurement of electronic, atomic and magnetic processes at a sub ps ( $10^{-12}$  s) time-scale, thus making it possible to temporarily disentangle cause-and-effect relations between coupled degrees of freedom. Based on this idea, ultrafast pump-probe spectroscopy is employed in order to study the dynamics of the electron-lattice interactions in the spin-state transition in  $\text{LaCoO}_3$  (**Paper I**) and the electron-lattice-spin couplings in the magnetic low-temperature phase of  $\text{La}_{1-x}\text{Ca}_x\text{MnO}_3$  (**Paper II**).

Inelastic light (Raman) scattering is a sensitive and local probe of the low energy quasiparticle spectrum, and provides unique insight in the detailed atomic structure and electron-phonon-spin interactions of correlated systems. The complicated structural evolution of three series of isovalently substituted  $\text{BiFeO}_3$  is studied with Raman spectroscopy in **Paper III**. In **Paper IV** and **V** the vibrational properties of  $\text{BaInO}_3\text{H}$  is studied as a function of temperature, providing the first phonon assignment and a detailed investigation of the hydrated-dry transition. Raman spectroscopy is also used in **Paper VI** in order to study the electron-phonon coupling in the new iron-pnictide class of high temperature superconductors.

# 2

## Structure and d-orbital Physics of Perovskites

In this chapter an introduction to the  $d$ -orbital physics shared by the transition metal perovskites studied in this thesis is presented. The aim is to explain the conceptual framework for understanding the large variations in physical properties arising from the interplay between atomic, magnetic and electronic structure. The chapter will first present the perovskite structure and the approximation of ligand field theory that attempts to explain the relative positions of the various energy levels in a transition metal (TM) complex. Then, the latter part of the chapter regards commonly used effective Hamiltonians for describing transition metal compounds together with a discussion about the relationship between structural parameters and electronic/magnetic properties in perovskite materials.

### 2.1 The Perovskite Structure

Materials belonging to the perovskite structure, with general chemical composition  $ABO_3$ , are amongst the most studied in condensed matter physics. From a physicist's point of view, this is largely due to the interplay between lattice, electronic, and spin degrees of freedom that allow for a variety of interesting and exotic properties.[8] The relative importance of the different degrees of freedom is very sensitive to both chemical substitution (on either the  $A$  or  $B$  site) and to external perturbations, i.e electric/magnetic field, temperature, or pressure. This leads to macroscopic properties, affected by relatively small perturbations, exemplified in this thesis by colossal magnetoresistance[1] ( $La_{1-x}Ca_xMnO_3$ ), spin-state transitions[2] ( $LaCoO_3$ ), and multiferroicity[9] ( $BiFeO_3$ ).

The ideal perovskite structure belongs to space group  $Pm\bar{3}m$  and consists

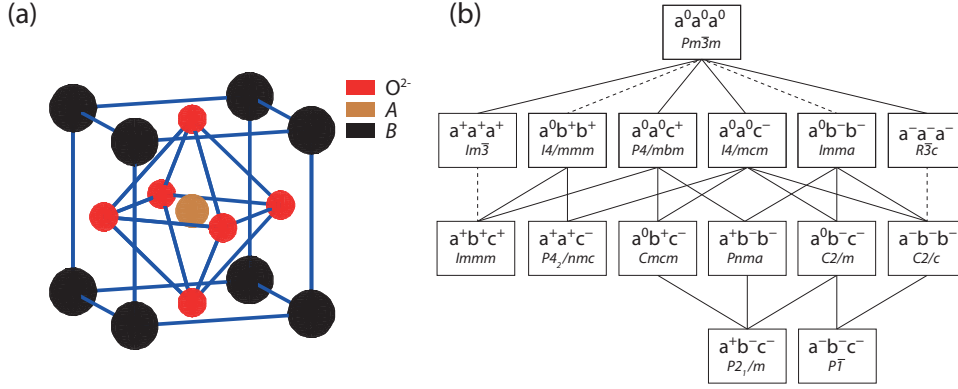


Figure 2.1: (a) The cubic perovskite structure in space group  $Pm\bar{3}m$ . (b) The allowed basic tilt systems and the corresponding space groups. Lines connecting two space groups indicate a subgroup relationship, where the lower of the two space groups is a subgroup of the upper and signifies possible second-order phase transitions. Dashed lines further indicate first-order transitions. (b) is reproduced from Howard[10].

of a cubic  $A$  lattice, within which the  $B$  and  $O^{2-}$  ions are positioned at the body centered and face centered sites respectively, as shown in Fig. 2.1(a).

The cubic  $Pm\bar{3}m$  structure is seldom realised in real materials. Deviations from  $Pm\bar{3}m$  can be decomposed into three basic distortions[10]: Octahedral tilts, octahedral distortions and translational  $A$ -site offsets. The perfect structure, and the deviations from it, can be parameterized via the tolerance factor  $t = (R_A + R_O)/\sqrt{2}(R_B + R_O)$ , where the  $R_x$  is the ionic radius of the respective species in  $ABO_3$ . The construction of  $t$  is purely geometric where  $t = 1$  is the condition for the perfect cubic perovskite.

When  $t < 1$ , there is a mismatch between the radii of  $A$  and  $B$  in such a way that the oxygen octahedra distorts and tilts in order to fit the  $A$  lattice; the structure goes from cubic to orthorhombic or rhombohedral. The oxygen tilts, being the most common distortion, are often described in Glazer notation[11], where a given tilt is specified as  $a^x b^y c^z$ , with  $\{x, y, z\} \in \{+, -, 0\}$ .  $a$ ,  $b$ , and  $c$  specifies along which crystal axis the tilt occurs and  $+$ ,  $-$ ,  $0$  specifies if the tilt is in-phase, anti-phase, or nonexistent respectively. As an example, the  $a^+a^+c^0$  tilt is in-phase with identical magnitude along both  $a$  and  $b$  while along  $c$  there is no tilt. A collection of the tilt systems and their group/sub-group relationships, relevant for the possibility of second order phase transitions, are collected in Fig. 2.1(b).

Relating to the perovskites investigated in this thesis, distortions of the compounds are collected in Table. 2.1. The way in which these distortions affects the physical properties by modifying the interactions within the material

is discussed in more detail in section 2.4.

Table 2.1: List of the structural distortions in the perovskite materials discussed in this thesis.

Material	Space Group	Tilt	Distortion	Offset
LaMnO <sub>3</sub>	<i>Pnma</i>	$a^+b^-b^-$	Jahn-Teller	–
LaFeO <sub>3</sub>	<i>Pnma</i>	$a^+b^-b^-$	–	–
LaCoO <sub>3</sub>	<i>R<math>\bar{3}c</math></i>	$a^-a^-a^-$	–	–
BiFeO <sub>3</sub>	<i>R<math>\bar{3}c</math></i>	$a^-a^-a^-$	–	<i>A</i> -site along (111)

## 2.2 Ligand Field Theory and Optical Transitions

The optical properties of solid state matter is determined by the allowed electronic excitations within the band structure. Interpreting data from optical spectroscopy thus require knowledge of the electronic bands and their symmetry properties. The number of allowed optical transitions and their rough relative positions can be obtained, via group theory, from ligand field theory without the need to first obtain knowledge about detailed material parameters.

### 2.2.1 Selection Rules

The metal-ligand bonding  $E_{ij} = \langle \phi_j | \mathcal{H}_0 | \phi_i \rangle$  between localized atomic wave functions give rise to the extended bands and is limited to between orbitals of the same symmetry  $i$ :  $E_{ij} \sim \delta_{ij}$ . The symmetries of the bands forms the basis for the discussion about the dipole allowed transitions that are pumped and probed in the time-resolved techniques utilized in **Paper I** and **Paper II**. A more general view of selection rules is also important in the context of the Raman spectroscopy technique, upon which **Papers III-VI** are based.

Generally, selection rules dictates the condition under which the matrix element  $\langle \psi_F | O | \psi_I \rangle = S$  between an initial state  $|\psi_I\rangle$  and final state  $\langle \psi_F|$  is non-zero. With the superscript  $\Gamma$  indicating the irreducible representation<sup>1</sup> of the initial/final state and operator  $O$ , the general selection rule is

$$\Gamma_F \subseteq \Gamma_O \otimes \Gamma_I, \quad (2.1)$$

or in other words: The final state must belong to a subset of the representation

<sup>1</sup>The condensed matter notation for the irreducible representations are such that  $a$  (and  $b$ ) denotes one dimensional,  $e$  two dimensional and  $t$  three dimensional representations.  $g$  and  $u$  signifies even (gerade in German) or odd (ungerade) with respect to the inversion operator. Further,  $a_{1g}$  is reserved for the fully symmetric representation. If the structure lacks a center of inversion, the distinction between  $a_{1g}$  and  $a_{1u}$  is lost, and thus  $Aa1$  is the symmetric representation.[12]

contained in the direct tensor product of the representations of the initial state with those of the operator  $O$ .

The light-matter interaction takes place through the Hamiltonian  $\mathcal{H}' \sim \mathbf{A} \cdot \mathbf{p}$  with  $\mathbf{A}$  the electromagnetic vector potential and  $\mathbf{p}$  the electron momentum operator.<sup>2</sup> Expanding  $\mathbf{A}$  in terms of the position operator  $\mathbf{x}$ , one obtains to zeroth order the dipole  $\mathcal{H}'_{DP} \sim \mathbf{A}_0 \cdot \mathbf{p}$ , and to first order the quadrupole  $\mathcal{H}'_{QP} \sim A_1 \mathbf{x} \cdot \mathbf{p}$ , Hamiltonians,[12] where  $\mathbf{A}_0$  and  $A_1$  are vector and scalar constants respectively. Because the wavelength of light is much smaller than lattice spacings, the light-matter dipole interaction is much stronger than the quadrupole interaction. The dipole operator transforms as a vector  $\Gamma_{\text{vec}}$  and the dipole selection rule is

$$\Gamma_F \subseteq \Gamma_{\text{vec}} \otimes \Gamma_I. \quad (2.2)$$

$\Gamma_{\text{vec}}$  contains only representation that are odd under spatial inversion (a vector changes sign under inversion  $x, y, z \rightarrow -x, -y, -z$ , hence it is odd), implying that dipole allowed transitions can only take place between states of opposite parity.

The quadrupole operator transforms as the even bilinear forms[12],  $xy, xz, yz, x^2 - y^2$ , and  $z^2$ . Quadrupole transition are thus only allowed between states of equal parity. Note that even if a particular transition is "parity allowed", it must be explicitly checked that the tensor product  $\Gamma_O \otimes \Gamma_I$  actually contains the representation of the final state. Neither the dipole or quadrupole operator acts on the spin degree of freedom and they are thus spin conserving transitions,  $\Delta S = 0$ . However, if for example the spin-orbit interaction  $\mathbf{l}_i \cdot \mathbf{s}_i$  is considered, there is now a possibility to act on the spin degree of the wave function and activate previously spin-forbidden transitions.[14, 15] Furthermore, the parity selection rules are relaxed in non-centrosymmetric complexes where the inversion operator is not part of the point group.

## 2.2.2 The Octahedral Energy Level Scheme

The energy-level scheme according to ligand field theory is obtained by combining atomic orbitals on the transition metal and ligands according to the group theoretical selection rules. Hence, the  $3d e_g$  orbitals will hybridize with the  $e_g$  orbitals from O  $2p \sigma$  to form a doublet consisting of one bonding and one anti-bonding level (denoted with  $*$ ) and the  $3d t_{2g}$  orbitals hybridizes with the  $\sigma$  and  $\pi t_{2g}$  orbitals from the oxygen to form bonding, anti-bonding and non-bonding levels. The remaining O  $2p$  orbitals hybridize with the unoccupied  $4s$  and  $4p$  on the transition metal, resulting in the energy level scheme in Fig. 2.2. The crystal field splitting  $10Dq$  within the  $d$ -orbitals is thus a direct consequence of the transformation properties and corresponds to the energy gap between the anti-bonding  $t_{2g}^*$  and  $e_g^*$ .

<sup>2</sup>Here, the  $\mathbf{A} \cdot \mathbf{A}$  term has been neglected, while for electronic Raman spectroscopy on metals for example, the  $\mathbf{A} \cdot \mathbf{A}$  term is of crucial importance.[13]

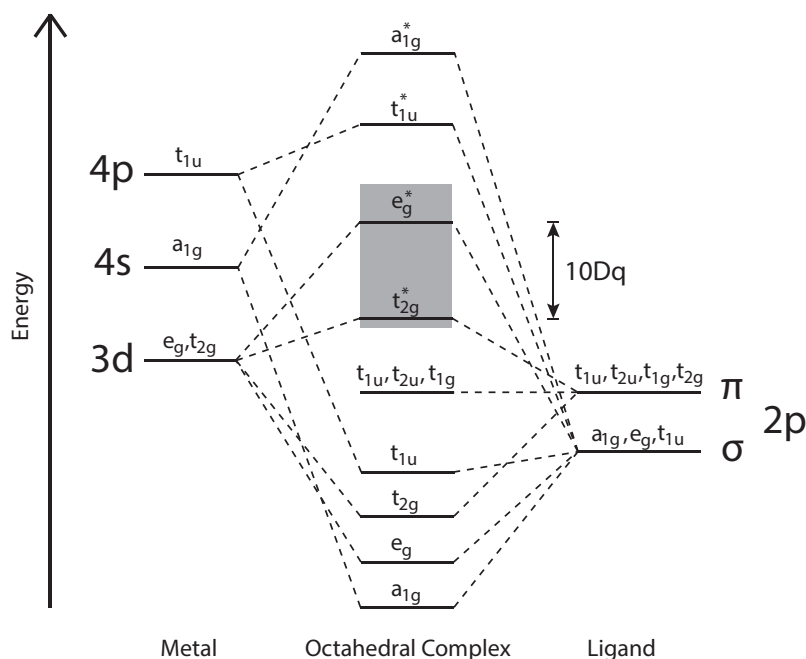


Figure 2.2: Energy level diagram for an octahedral oxygen - transition metal complex based on the group theoretically allowed hybridizations of orbitals. The shaded area highlights the "d-orbitals" and the crystal field splitting commonly discussed in the context of transition metal perovskites.

In the crystal, as opposed to the isolated complex, the energy levels will broaden and form extended energy bands.[16] A complication arising in the solid is the possibility of "inter-cluster" transitions between adjacent TM-ions, where the  $d-d$  repulsion  $U$  (discussed in Sec. 2.3) needs to be taken into account in a configuration-interaction cluster model.[8, 17, 18] The assignment of optical transitions is thus not as simple as the perfect complex makes you believe. However, the formally allowed dipole transitions are usually much stronger than the transitions that becomes weakly-allowed by the effects discussed above. Still, the weakly-allowed transition can be very important when they are responsible for the low energy optical transitions, as is the case for the  $d-d$  transitions in the manganites studied in **Paper II**. [19]

## 2.3 The Hubbard Model

The fact that the varied set of exotic properties of perovskites arises from essentially the same physics offers a fundamental challenge to our ability to theoretically model condensed matter systems, where one should expect a single theoretical framework to explain the essence of more or less all the investigated transition metal perovskites. To this end, the Hubbard model is the starting

Table 2.2: Extension terms to the tight-binding model, including Hamiltonian[20], and physical meaning.  $\vec{S}_i$  and  $\vec{\sigma}_i$  denotes spin operators for the  $e_g$  and  $t_{2g}$  levels,  $Q_{2i}$  ( $Q_{3i}$ ) are the normal coordinates of the octahedral distortion and  $T_i$  are pseudo-spin operators defined from  $\hat{c}$  and  $\hat{c}^\dagger$ . [8, 20]

Term	Hamiltonian	Physical effect
Coulomb repulsion	$U \sum_i \hat{n}_{i\uparrow} \hat{n}_{i\downarrow}$	Energy cost of double occupancy of an orbital/site.
Hunds coupling	$-J_H \sum_i \vec{S}_i \cdot \vec{\sigma}_i$	Energy is required to have two electron on the same site with opposite spin.
Dzyaloshinskii-Moriya	$\sum_{\langle ij \rangle} D_{ij} \vec{S}_i \times \vec{S}_j$	Anisotropic exchange, favoring a canted spin arrangement.
Superexchange	$\sum_{\langle ij \rangle} J_{ij} \vec{S}_i \cdot \vec{S}_j$	Isotropic exchange, favoring FM or AFM phases.
Jahn-Teller	$2g(Q_{2i}T_i^x + Q_{3i}T_i^z) + k_{JT}/2(Q_{2i}^2 + Q_{3i}^2)$	Electron-phonon coupling, relating structural distortions to the orbital occupancy.

point for most of the effective Hamiltonian introduced as the basis for such a description. Here, a short introduction of the Hubbard model is given before the next section explores some basic materials systematics.

An effective Hamiltonian is an approximation of the full Hamiltonian that only contains the low-energy degrees of freedom judged relevant in the context at hand. The most basic example of an effective Hamiltonian is the tight-binding model

$$\mathcal{H}_{TB} = - \sum_{\langle ij \rangle} t_{ij} \hat{c}_i^\dagger \hat{c}_j \quad (2.3)$$

that describes the possibility for electrons to jump from state  $i$  to state  $j$ , parameterized by the hopping integral  $t_{ij}$ . Because the bands close to the Fermi surface in transition metal perovskites are made out of electrons in the  $e_g^*$  and  $t_{2g}^*$  levels it is often assumed that these are the only relevant electrons. The effective description should therefore include the five  $d$ -orbitals on the transition metal ion in addition to the  $t_{2g}$  and  $e_g$  combinations of ligand  $p$  orbitals.

However, it is often possible to significantly reduce the number of orbitals to consider. If the crystal field splitting  $10Dq$  between the  $e_g^*$  and  $t_{2g}^*$  levels is large, one can consider that only the  $e_g$  electrons are able to move close to the Fermi level. Because the  $e_g$  levels only hybridize with the oxygen  $\sigma$  orbitals, the number of orbitals to consider is reduced to three (two  $e_g$  plus one O  $\sigma$ ). For example, the perovskite  $\text{LaMnO}_3$  has only one  $e_g$  electron on each site, and

in this case it is common to consider only *one* orbital on each site. The hopping integral for this  $e_g$  electron then represents an effective Mn-Mn hopping with the bridging oxygen only included implicitly.

One of the most important models based on the tight-binding formulation is the Hubbard model, obtained by reducing the tight-binding Hamiltonian to one orbital per site and including inter-site electron-electron interactions:

$$\mathcal{H}_H = - \sum_{\langle ij \rangle \sigma} t_{ij} \hat{c}_{i\sigma}^\dagger \hat{c}_{j\sigma} + U \sum_i \hat{n}_{i\uparrow} \hat{n}_{i\downarrow}, \quad (2.4)$$

with the spin index  $\sigma = \{\uparrow, \downarrow\}$  explicit, so that the single orbital on site  $i$  now has room for two electrons, and introduced the number operator  $\hat{n}_i = \hat{c}_i^\dagger \hat{c}_i$  that counts the number of electrons in state  $i$ .

The effect of the  $U$  term is to introduce an electrostatic energy requirement for double occupancy of an orbital, and with this addition the Hubbard model manages to capture the transition from the metal to the Mott insulator. By relaxing the restriction of one orbital per site, the Hubbard model can be extended to include all the relevant interactions such as the intra-site Hund's coupling and other exchange mechanisms encoded in the full electrostatic interaction term  $V_{ijkl}$ . [8, 20] With these terms in place, the interatomic superexchange interactions, stabilizing ferromagnetic/antiferromagnetic phases, are obtained perturbatively as virtual transfers involving higher powers of  $t_{ij}$ . [21] In Table 2.2 a list of commonly encountered extensions to the Hubbard model in relation to perovskites is provided. The Coulomb and exchange interactions included in such multi orbital models can be related to the energy level splittings discussed in Section 2.2. A combination of the ligand field and the effective Hamiltonian approach then provides a powerful framework by which many of the interesting properties of transition metal perovskites can be understood.

## 2.4 Structural Effects on the Electronic and Magnetic Properties

In this section a combination of the ligand-field and effective Hamiltonian approach is used in order to understand the effect of structural distortions and atomic substitution on the electronic and magnetic properties of transition metal perovskites. This includes the ability to more or less continually tune the  $t$  and  $U$  parameters with atomic substitution and external perturbations (manganites, **Paper II**), the interplay between intraatomic exchange and the ligand field splitting (cobaltites, **Paper I**) and pure symmetry considerations that limit the magnetic couplings allowed (BiFeO<sub>3</sub>, **Paper III**).

The relative strength of the hopping integral  $t$  compared to the on-site repulsion  $U$  is strongly dependent on the exact lattice structure. In general,  $t$  increases with increasing  $3d - O 2p$  overlap and to first order the relationship is

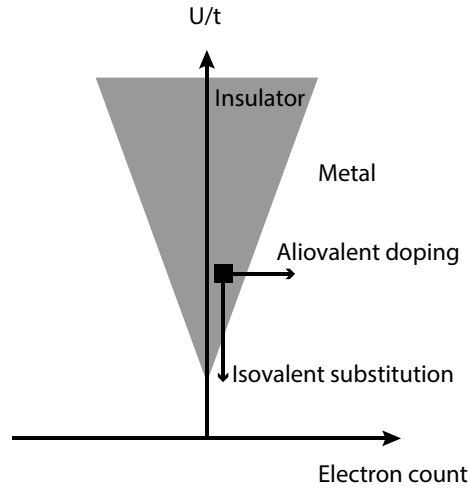


Figure 2.3: Schematic of the insulator-metal transition in the Hubbard model. From the point in the parameter space indicated with the black square it is possible to induce the insulator to metal transition in the two ways discussed in the text: By "band-width control" or by "filling control", exemplified with isovalent substitution and aliovalent doping on the *A*-site respectively. The figure is inspired and redrawn from Fig. 1 in Ref [8].

linear:  $t \sim \cos(\theta)^2$ , with  $\theta$  the TM-O-TM angle.[8] The reduction of  $t$  with decreasing  $\theta$  narrows the  $d$ - $p$  hybridization bandwidth and consequently increases the relative importance of the intersite repulsion  $U$  - the ratio  $U/t$  increases. In this way, isovalent substitution on the *A*-site, pressure, or temperature can have large effects on the electronic structure through a change in the tolerance factor and hence  $U/t$  via  $\theta$ . As an example, the perovskite  $R\text{NiO}_3$  is driven from a metal towards an insulator as  $R$  changes from La to Y following the change in tolerance factor from 0.94 to 0.88.[22] Because the superexchange interactions contains powers of  $t_{ij}$ , also the magnetic coupling decrease with decreasing  $\theta$  and a resulting change in the tendency to order magnetically should also be expected for isovalent substitution.

Aliovalent substitution (doping) on the *A*-site more drastically modifies both the electronic and magnetic structure by changing the  $d$ -electron count on the *B*-site. Starting at the Mott-insulating phase with one effective electron per site in the Hubbard model, a change in the electron filling away from one electron per site causes an increase in the number of possible electron transfers unaffected by  $U$  resulting in a insulator-metal transition at high enough doping. At the same time, the change in electron count might change the sign of the superexchange interaction according to the Goodenough-Kanamori rules[23, 24] with a resulting tendency for the magnetic order to go from antiferromagnetic to ferromagnetic.

The two routes (band-width control and filling control) to drive the Mott

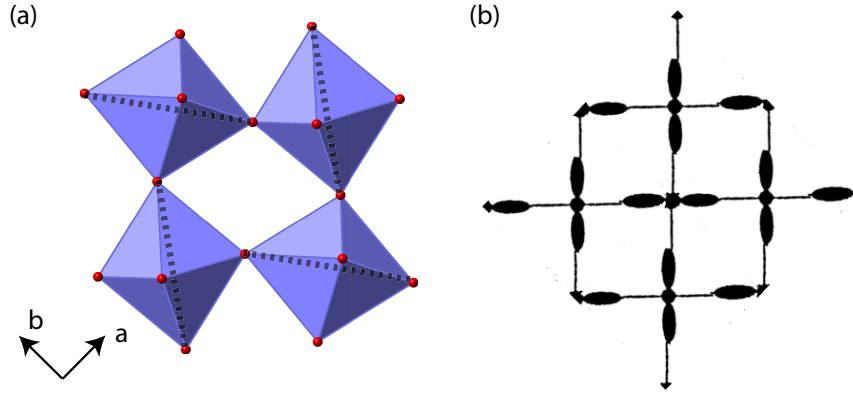


Figure 2.4: Jahn-Teller distortions in  $\text{LaMnO}_3$  as shown in (a) the octahedral elongation parallel to the broken lines and in (b) the underlying orbital ordering of the single  $e_g$  electron on each Mn site. Note that the schematic orbital ordering in (b) assumes  $180^\circ$  Mn-O-Mn angles, while the real structure in (a) exhibit a Mn-O-Mn angle substantially smaller than  $180^\circ$ . (b) is adapted from Ref. [20].

insulator into a metal, here exemplified by doping and isovalent substitution, are summarized in the Hubbard-model phase diagram, Fig. 2.3.

Besides the geometrical effect parameterized by the tolerance factor, the Jahn-Teller theorem[25] states that any configuration in which an electron can occupy one of several degenerate orbitals will undergo a spontaneous symmetry breaking through the reduction of lattice symmetry. For example, imagine the case of a cubic TM- $\text{O}_6$  complex with electronic configuration  $t_{2g}^3 e_g^1$ . The  $e_g$  electron can occupy any one of the two  $e_g$  orbitals as they are degenerate in energy. Now, as explained by the Jahn-Teller theorem, the oxygen octahedra will distort so that the degeneracy between  $d_{x^2-y^2}$  and  $d_{3z^2-r^2}$  is lifted and the energy of the occupied orbital becomes lower compared to without the Jahn-Teller effect.

In the  $t_{2g}^3 e_g^1$  configuration of  $\text{LaMnO}_3$ , the Jahn-Teller effect causes an elongation along  $z$  so that  $d_{3z^2-r^2}$  is reduced in energy. Adjacent octahedra will exhibit an elongation with  $90^\circ$  between each other, giving rise to the orbitally ordered arrangement shown in Fig. 2.4. Such an orbitally ordered state further localizes the  $e_g$  electrons, and contribute to the results presented in **Paper II**.

As was seen above, the five degenerate  $d$ -orbitals split into the  $t_{2g}$  and  $e_g$  levels in the perovskite structure. Due to the interionic Hund-coupling  $J_H$ , the lowest energy is obtained by placing the electrons with parallel spins and in separate orbitals.[14] As a consequence, the three first  $d$ -electrons at a transition metal site with octahedral coordination are always placed in the  $t_{2g}^3$  arrangement with their spins mutually parallel. The relative strengths of the crystal field splitting  $\Delta_{CF}$  and  $J_H$  determines then if a fourth electron produces  $t_{2g}^3 e_g$ ,

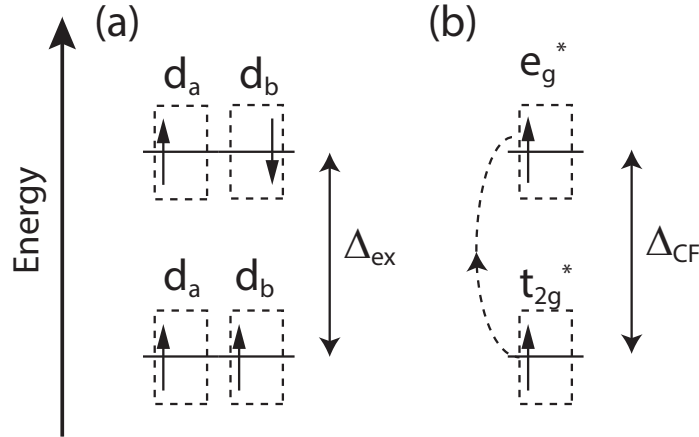


Figure 2.5: (a) Schematic of the crystal field splitting ( $\Delta_{\text{CF}}$ ) and Hund exchange ( $\Delta_{\text{ex}}$ ) energies.  $\Delta_{\text{ex}}$  is the additional energy required for two spins to be anti-parallel as opposed to parallel.  $\Delta_{\text{CF}}$  is the energy required to promote an electron from the  $t_{2g}$  to the  $e_g$  band. (b) The spin arrangements in the low-spin and high-spin configurations of  $\text{LaCoO}_3$ , differing by an energy gap  $\Delta \sim \Delta_{\text{CF}} - \Delta_{\text{ex}}$ . In the solid, the  $p$ - $d$  bonding broadens the strongly hybridized  $e_g$  levels into bands with bandwidth  $W$ , altering the spin-gap to  $\Delta \sim \Delta_{\text{CF}} - W/2 - \Delta_{\text{ex}}$ .<sup>[26]</sup>

all spins parallel ( $J_H > \Delta_{\text{CF}}$ ) or  $t_{2g}^4 e_g^0$  ( $J_H < \Delta_{\text{CF}}$ ), see Fig. 2.5. The former case is the high spin (HS) and the latter is the low spin (LS) configuration.

$J_H$  is an intraionic effect and is as such practically independent on the atomic arrangement around the transition metal.  $\Delta_{\text{CF}}$  depends on the TM-O distance, which gives the pure crystal field splitting  $\Delta$ , and also on the TM-O-TM angle that affects the bandwidths  $W$ . When the values  $J_H$  and  $\Delta_{\text{CF}}$  are similar in magnitude, small structural changes can thus drive the system to be either HS or LS. This phenomena is investigated in **Paper I**.

# 3

## Investigated Materials

This chapter gives a short review of the transition metal perovskites and ironpnictides investigated in this thesis. Both these classes of materials exhibit peculiar properties that are ultimately produced by strong correlations between electrons. The perovskites investigated here are classified according to their  $B$  site transition metal and fall under *manganites*, *cobaltites*, and *ferrites*. In addition the pseudo-perovskite of hydrated *brownmillerites* is investigated.

The most striking property of the manganites is the colossal magnetoresistance (CMR in short), [1, 27, 28] but essentially all ground state properties are affected, albeit in a more subtle way, by strong electron correlations. [20, 29, 30] Cobaltites exhibit strong electron-lattice coupling that gives rise to a complicated spin-state evolution as a function of temperature, pressure, and atomic substitution. Regarding the multiferroic ferrites and proton-conducting brownmillerites the focus is more specifically on the structure-composition interplay, which in many respects determine, by symmetry arguments, the most interesting properties of these materials.

### 3.1 Manganites

Manganites,  $(Re, A)MnO_3$  with  $Re$  being a rare earth (typically La) and  $A$  an alkaline element, was first studied in 1950 by Jonker and Van Santen. [31] They studied compounds based on  $LaMnO_3$ , with different amount of trivalent La substituted by divalent Ca, Sr or Ba. In all three cases they found an intriguing coincidence between a insulator-metal transition and a transition between paramagnetic and ferromagnetic states.

An explanation for this coincidence was found rather quickly in the *double exchange* mechanism discovered by Zener [32, 33] and elaborated on by Anderson and Hasegawa [34], and DeGennes. [35] Due to the great success of this explanation, the interest in manganites waned, only to be reignited in the

1990's when colossal magnetoresistance effects, whereby the resistance is reduced by a factor up to  $10^6$  after the application of a magnetic field, was discovered.[1, 27, 28] During the almost 20 years since the awakened interest in manganites, it has been realized that the physics of manganites is extremely rich and complex, with a satisfactory theoretical understanding being almost as elusive as for the high temperature superconductors.

The rich physics of manganites stems to a large extent from competition between different microscopic phenomena that happens to lie very close in energy, a theme that seems to be generic for the behavior of strongly correlated materials.[29, 30] This results in different structural, magnetic and electronic phases that are closely related in energy and the existence of intrinsic phase separation. Although a complete understanding of the physics of manganites is yet to be obtained, it is understood that in order to explain the observed features, strong correlations between different degrees of freedom have to be taken into account, especially electron-electron and electron-lattice effects.[36, 37]

As mentioned above, the first sign of interesting physics in manganites was the observation of a simultaneous occurrence of the insulator-metal and the paramagnetic-ferromagnetic transitions. This concurrence is only observed in the mixed valence manganites, with  $\text{La}_{1-x}\text{Ca}_x\text{MnO}_3$  as the prototypical example. The parent compound  $\text{LaMnO}_3$  crystallizes in the  $Pnma$  space group and is a semiconductor that goes through a phase transition from a paramagnetic to an antiferromagnetic phase at the Neel temperature  $T_n \sim 150\text{K}$ . [20, 38, 39] The antiferromagnetic state is of the A-type, where the spins on the Mn ions form alternating ferromagnetic layers in the z-direction.[38] The static Jahn-Teller distortion stabilizes a checkerboard pattern in the occupied  $e_g$  orbital below 700K,[40, 41] see Fig. 2.4.

The effects of such a aliovalent substitution was discussed in Sec. 2.4 and can be summarized as an increased metallic tendency as holes are introduced in the Hubbard model as well as increased ferromagnetic couplings. However, the room temperature state of  $\text{La}_{1-x}\text{Ca}_x\text{MnO}_3$  is still insulating over the whole doping range.

The intersite  $d_{\uparrow}^4-d_{\uparrow}^4$  transition is of the order a few eV (in  $\text{LaMnO}_3$ , which is semiconducting, the bandgap lies on the edge of this crystal field excitation and is approximately 1.2eV[42]), while the  $d_{\uparrow}^4-d_{\downarrow}^4$  transition is substantially higher.[19, 43, 44] The  $d-d$  transition from an occupied to an unoccupied  $e_g$  orbital, i.e the  $d_{\uparrow}^4-d_{\uparrow}^3$  transition, on the other hand may occur spontaneously and is the mechanism by which the hole doped manganites becomes conducting. This transport of charge is mediated via the bridging  $\text{O}^{2-}$  ion and is called double exchange.[32, 33, 34, 35]

The double exchange mechanism can be thought of as the real analogue to the virtual superexchange interaction, where two successive Mn-O charge transfers are only allowed by the Pauli principle if the Mn ions are ferromagnetically aligned. see Fig. 3.1. The amplitude of the double exchange hopping is found

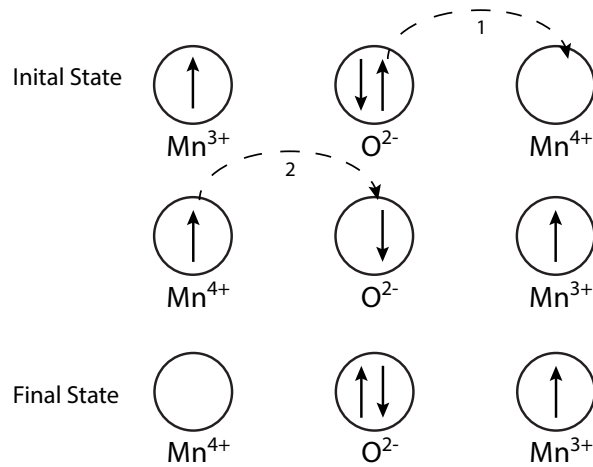


Figure 3.1: Illustration of the double exchange mechanism. A combination of the Pauli principle on the bridging O  $2p$  orbital and Hund's coupling between the  $t_{2g}$  and  $e_g$  orbitals on the Mn ions prohibits the simultaneous (1)  $O^{2-}-Mn^{4+}$  and (2)  $Mn^{3+}-O^{1-}$  charge transfer unless the Mn ions are ferromagnetically aligned.

to be proportional to  $\cos^2 \theta$  where  $\theta$  is the angle between the Mn ions through the oxygen ion,[34] just as for superexchange. Although the double exchange mechanism, visualized in Fig. 3.1, gives a qualitative explanation for the magnetoresistance effects in manganites, the colossal magnitude of this effect can not be explained by invoking only double exchange.[36] To fully account for the magnitude of the magnetoresistance effect, electron-lattice coupling and disorder effects intrinsic to manganites has to be considered. Several types of disorder come into play, both at the lattice and electronic level.[45] When doping the trivalent *Re* site with a divalent *A* element, the resulting alloy will exhibit colossal magnetoresistance only if the placement of the *A* ions are random in the lattice. In experiments where nominally the same compound have been manufactured, but with an ordered arrangement of *Re* and *A* ions, the magnetoresistance effect has been shown to disappear.[46]

These, to just name a few, experimental findings together with strong effects from both static and dynamic Jahn-Teller distortions[25, 45] and the combination of electron microscopy imaging and theoretical models that predict intrinsic phase separations show unambiguously that disorder is crucial for the complex physics observed in manganites.[20, 47, 48]

During the last fifteen years, rapid developments in ultrafast laser sources have led to powerful new experimental methods that directly probes the dynamic interplay between different degrees of freedom. In **Paper II** such ps dynamics, following the resonant excitation of the intersite  $d_{\uparrow}^4-d_{\downarrow}^4$  transition, is investigated as a function of probing wavelength. As a further example, it has been observed that by selectively exciting individual Mn-O stretching modes

with infrared light, a manganite can be pushed from a stable insulating to a metastable metallic state by directly disordering the oxygen octahedra on a femtosecond time scale,[49] demonstrating the ability to directly control the complicated phase diagram in manganites.

## 3.2 BiFeO<sub>3</sub> and Multiferroicity

Multiferroic compounds exhibit a coincidence of ordered (ferro or antiferro) magnetic and electric phases. Ferroelectricity occurs when there exists a macroscopic polarization with an origin in non-centrosymmetric displacements of charged ions in the unit cell. Due to the ionic displacements a finite dipole moment, adding up to a macroscopic polarization in the bulk, will be associated with each unit cell.

Multiferroic transition metal perovskites are relatively rare and the reason for this can be understood in the  $d$ -orbital physics.[50] It has been noticed that ferroelectricity, due to off-center  $B$  site displacements, occurs most frequently in  $d^0$  compounds.[50] This might be due to the lack of (centrosymmetric) anisotropic lattice distortions, for example Jahn-Teller effects, arising from the highly directional  $d$ -orbitals that compete, and overcome, the tendency for  $B$ -site displacements.[50] On the other hand, magnetism in transition metal perovskites arises almost exclusively from the  $B$ -site transition metal  $d$ -orbital electrons. From these simple considerations it is natural that the mutual existence of a macroscopic polarization from the translational  $B$ -site offset (observed in  $d^0$  compounds) and ordered magnetic spins (which excludes a  $d^0$  configuration) becomes suppressed.

However, exceptions to the rules above exist, as exemplified not least by BiFeO<sub>3</sub>, which is the only known room temperature multiferroic compound.[51] Although multiferroicity at room temperature was discovered in BiFeO<sub>3</sub> already in the 1960's[52], it was the discovery of magnetoelectric effects in thin-films that made the scientific interest in this material to surge a decade ago.[53]

The key behind the multiferroic phase in BiFeO<sub>3</sub> is that, due to the lone-pair nature of the Bi<sup>3+</sup>  $6s^2$  configuration, it is the  $A$  site ion that is responsible for the polarization. The lone-pair describes the tendency for the Bi  $6s^2$  electrons to form an anisotropic, directed, charge lobe that is compensated, in BiFeO<sub>3</sub>, by a translational offset of the Bi ion. The resulting non-centrosymmetric atomic arrangement gives rise to the macroscopic polarization.

The magnetism in BiFeO<sub>3</sub> stems from the high-spin  $t_{2g}^3 e_g^2$  Fe<sup>3+</sup> ion[54], where the spins at adjacent Fe sites order in the G-type (checkerboard) antiferromagnetic arrangement, upon which a both canted and cycloidally modulated spin-order is superimposed.[9, 55] BiFeO<sub>3</sub> crystallizes in the  $R3c$  structure that, besides the translational Bi offset along [111] in the pseudo-cubic setting, differs from the ideal cubic structure by an antiphase tilt of the oxygen octahedra along all three directions ( $a^-a^-a^-$  in Glazer notation[11]). In Fig. 3.2 the

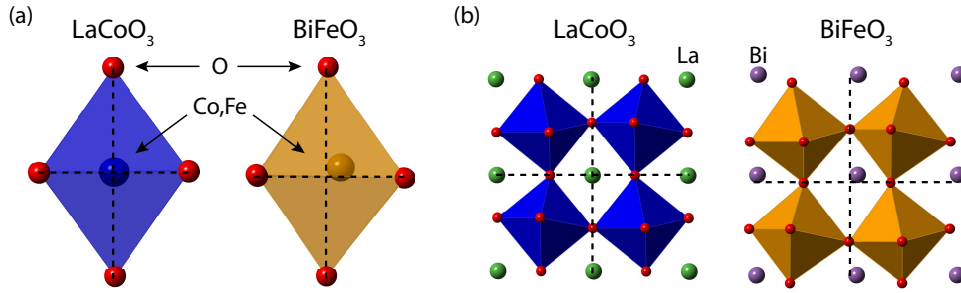


Figure 3.2: Comparison of the *B*-site (a) and *A*-site (b) position inside the oxygen octahedra in centrosymmetric  $R\bar{3}c$  LaCoO<sub>3</sub> [56] and non-centrosymmetric  $R3c$  BiFeO<sub>3</sub> [57]. The broken lines serves as a guide for the eye to the center of symmetry. In LaCoO<sub>3</sub> all atoms are positioned symmetrically around these lines, but in BiFeO<sub>3</sub> both the Bi and Fe atoms clearly breaks the inversion symmetry.

non-centrosymmetric atomic positions in BiFeO<sub>3</sub> is shown in comparison with the centrosymmetric positions in the  $a^-a^-a^-$  tilt structure of LaCoO<sub>3</sub>. Note that both the Bi and Fe ions are disturbed from the corresponding symmetric La and Co positions in LaCoO<sub>3</sub>.

The presence of both magnetic ordering and macroscopic polarization opens up the exciting possibility of magnetoelectric effects, whereupon the polarization can be controlled with an applied magnetic field and vice versa.[58] Controlling the electric and magnetic states in this way would provide a whole new class of magnetoelectric devices, for example magnetic memories that can be written with electric fields.[9] However, the first order magnetoelectric effect, coupling the polarization  $P$  to an applied magnetic field  $H$  and the magnetization  $M$  to an electric field  $E$  through

$$P_i = \alpha_{ij} H_j \quad (3.1)$$

$$M_i = \beta_{ij} E_j, \quad (3.2)$$

averages to zero due to the presence of the spin cycloid. Until recently the suppression of the spin cycloid was thought to be a necessary prerequisite for obtaining magnetoelectric effects in BiFeO<sub>3</sub>. [51] Suppression of the spin cycloid was indeed found in thin-films, together with the activation of the first order magnetoelectric effects,[59, 60] and by atomic substitution on the Fe site.[61]

An additional effect of atomic substitution, either on the Bi or Fe site, is the tendency to drive the crystal structure away from the non-centrosymmetric  $R3c$ . Together with the tendency for phase separation and substitution inhomogeneities, the initial reports[59] of substitution induced enhancements of magnetoelectric couplings should be viewed with scepticism. Indeed, more recent studies have suggested that phase separation into ferroelectric  $R3c$  domains and

Table 3.1: Summary of the observed space groups as a function of isovalent substitution.

<b>Bi<sub>1-x</sub>Tb<sub>x</sub>FeO<sub>3</sub></b>	
$0 \leq x \leq 0.1$	<i>R3c</i>
$0.125 \leq x \leq 0.15$	<i>R3c + Pnma</i>
$0.175 \leq x \leq 1$	<i>Pnma</i>
<b>Bi<sub>1-x</sub>La<sub>x</sub>FeO<sub>3</sub></b>	
$0 \leq x \leq 0.1$	<i>R3c</i>
$0.15 \leq x \leq 0.175$	<i>R3c + PbZrO<sub>3</sub>-type</i>
$0.2 \leq x \leq 0.4$	<i>PbZrO<sub>3</sub>-type</i>
$0.5 \leq x \leq 1$	<i>Pnma</i>
<b>Bi<sub>0.9</sub>Sm<sub>0.1</sub>Fe<sub>1-x</sub>Mn<sub>x</sub>O<sub>3</sub></b>	
$x = 0$	<i>R3c</i>
$x = 0.15$	<i>R3c + Imma</i>
$x = 0.3$	<i>Imma</i>

magnetic orthorhombic domains with destroyed spin cycloid together gives the impression of enhanced magnetoelectric effects when the electric and magnetic characteristics are measured separately.[62]

Putting aside the connection with magnetism, the structural transitions themselves as a function of atomic substitution in BiFeO<sub>3</sub> has proven to be complicated to unravel. However, the interest in substituted BiFeO<sub>3</sub> stems not only from the aforementioned connection to magnetoelectric effects, but is also due to the compositional instability of BiFeO<sub>3</sub>, which has been suggested to only be metastable in ambient atmosphere.[9]

Upon isovalent substitution on the *A*-site, disorder is introduced which eventually leads to a decoherence of the Bi lone-pair and a concurrent change in space group from the polar *R3c* to a non-polar space group. The route from the polar to the non-polar symmetries depends greatly on which substituting element is used, both in relation to its concentration and ionic size.

La substitution is a particularly interesting, and complicated, case as the small change in ionic size, from 116 pm to 117 pm between La<sup>3+</sup> and Bi<sup>3+</sup>, [9, 63] makes dilution of the lone pair the main effect of substitution. Several studies on the relation between La-substitution and structure have been published, often with conflicting results.[59, 62, 64, 65, 66] Increasing the ionic size difference, as for example with Tb<sup>3+</sup> (ionic radius 104 pm), will introduce significant lattice distortions as a direct consequence and thus no intermediate structures between the *R3c* of BiFeO<sub>3</sub> and *Pnma* of (La,Tb)FeO<sub>3</sub> will be observed.[67] The space-groups observed as a function of isovalent substitution are summarized in Table. 3.1 for the compounds studied in Paper III.

Most of the structural studies on substituted BiFeO<sub>3</sub> are based on diffraction techniques and very few spectroscopic studies have been published. One

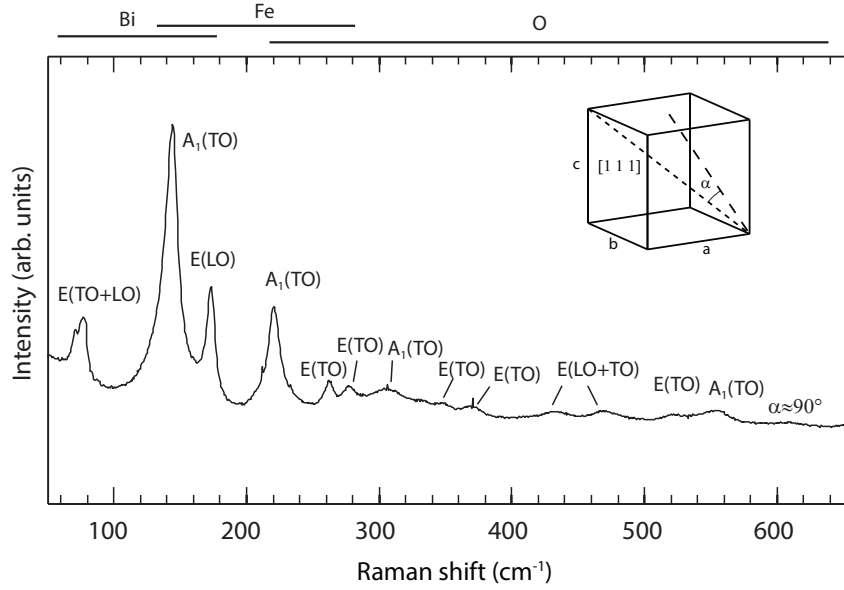


Figure 3.3: First order unpolarized Raman spectrum of BiFeO<sub>3</sub>. The frequency regions indicated with atomic labels above the figure shows the main atomic species involved in the vibrations.

possible reason for this is the controversies surrounding the phonon assignments in BiFeO<sub>3</sub>. [68, 69] The  $\Gamma$ -point phonon content in BiFeO<sub>3</sub> is  $5A_1 + 5A_2 + 10E$ . Out of these one  $A_1$  and one  $E$  corresponds to the three acoustic modes. Out of the remaining modes, the  $A_2$  are silent in both IR and Raman, while the  $A_1$  and  $E$  are active in both techniques.

The Raman spectra of BiFeO<sub>3</sub>, shown in Fig. 3.3 will thus include  $4A_1 + 9E = 13$  Raman active phonons. However, the spontaneous polarization of BiFeO<sub>3</sub> give rise to an angular phonon dispersion, where the frequency and irreducible representation of a given mode gradually changes as a function of angle  $\alpha$  between the incident light and the direction of polarization. [13] In addition, the doubly degenerate  $E$  modes split into one TO branch and one LO branch that coincides in frequency only when  $\alpha = 0$ .

Depending on the plane along which the crystal is cut, and the angle between the incident laser light and face-normal, phonon assignments that differ both in mode frequencies, the associated irreducible representations, and the number of modes will be obtained. A consistent assignment requires the full dispersion curve, given by measurements at several angles  $\alpha$ . Such measurements on BiFeO<sub>3</sub> have been performed [69] and provide, together with DFT calculations [70, 71], the basis for the, in my opinion, most reliable BiFeO<sub>3</sub> phonon assignments so far.

In **Paper III** the first comprehensive Raman study on isovalently substituted BiFeO<sub>3</sub> is presented and we (1) extract additional information about the

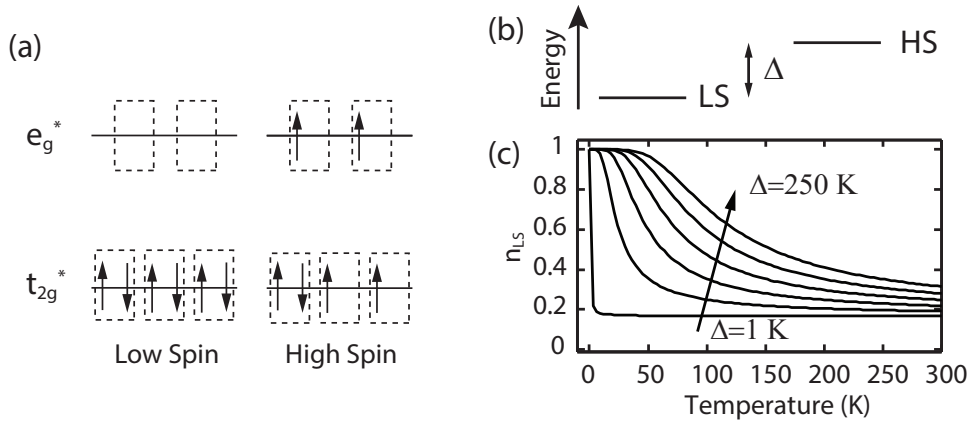


Figure 3.4: (a) The spin arrangements in the low-spin and high-spin configurations of  $\text{LaCoO}_3$ , differing by an energy gap  $\Delta \sim \Delta_{\text{CF}} - \Delta_{\text{ex}}$  as shown in (b). In the solid, the  $p$ - $d$  bonding broadens the strongly hybridized  $e_g$  levels into bands with bandwidth  $W$ , altering the spin-gap to  $\Delta \sim \Delta_{\text{CF}} - W/2 - \Delta_{\text{ex}}$ . [74] (c)  $n_{LS}$  as a function of temperature for equidistant values of  $\Delta$  between 1 and 250 K according to Eq. 3.3, assuming an orbital singlet HS excited state ( $Z = 5$ ).

phonon content by the use of small amounts of isovalent substitution on the Bi site, and (2) follow the structural transitions, and assign the main spectral features from  $R3c$  to  $Pnma$  via the incommensurate  $\text{PbZrO}_3$ -type structure.

### 3.3 Spin-State Transitions in $\text{LaCoO}_3$

In recent years  $\text{LaCoO}_3$  has received considerable attention both as a cathode material in solid oxide fuel cells [72] and for its catalytic properties [7]. Besides its potential in applications,  $\text{LaCoO}_3$  has been thoroughly investigated due to its magnetic properties that have puzzled researchers ever since the first studies in the 1950's.

In the ground state,  $\text{LaCoO}_3$  is a nonmagnetic insulator with rhombohedral space group  $R\bar{3}c$  and low-spin (LS)  $d$ -orbital occupancy  $t_{2g}^6 e_g^0$ . [8] The fundamental interest in this material comes from the gradual spin-state transition observed at  $\sim 100$  K [2, 73] which has been discussed to be either from LS to intermediate spin (IS)  $t_{2g}^5 e_g^1$  ( $S=1$ ) or from LS to high-spin (HS)  $t_{2g}^4 e_g^2$  ( $S=2$ ).

The driving mechanism behind the spin-state transition is visualized in Fig. 3.4 and depends on the similarly sized crystal field splitting  $\Delta_{\text{CF}}$  and intraionic exchange energy  $\Delta_{\text{ex}}$ , resulting in an extraordinary small spin-gap  $\Delta \sim \Delta_{\text{CF}} - \Delta_{\text{ex}}$  on the order of 200 K ( $\sim 17$  meV). For comparison, the spin-gap in  $\text{LaMnO}_3$  is on the order 1 eV, [20, 43] approximately a factor of 50 larger than the gap in  $\text{LaCoO}_3$ .

The simplest way to model the LS-HS transition is by a thermal LS popu-

lation given by Fermi statistics:[75, 76]

$$n_{\text{LS}}(T) = \frac{1}{1 + Z \exp(-\Delta/T)}, \quad (3.3)$$

where  $Z = (2S+1)\eta$  is the combined spin  $(2S+1)$  and orbital  $(\eta)$  degeneracy of the excited state.  $S$  is the total spin of the excited state and  $\eta$  varies depending on structurally induced energy splittings within the  $t_{2g}$  and  $e_g$  levels.  $n_{\text{LS}}(T)$  according to Eq. 3.3 can be seen in Fig. 3.4(c) for different values of  $\Delta$  between 1 and 250 K.

The earliest accounts for the spin-state transition was based on the HS picture, but the theoretical discovery of a favorable IS state[77] shifted the interpretations away from the HS and towards the IS picture.[74, 76, 78, 79, 80, 81] However, often the experiments still favored the HS picture.[82, 83, 84, 85, 86] The nature of the excited spin-state is still a controversial issue and supposedly unambiguous evidence has been presented for both the IS and HS spin states,[83, 87] although the newest reports seems to favor a HS state.[88]

A new route to understanding the spin-states in LaCoO<sub>3</sub> has been given by the recent discovery of a ferromagnetic (FM) state at low temperature in epitaxially grown LaCoO<sub>3</sub> thin films,[89, 90, 91, 92, 93, 94, 95, 96] implying a sizeable fraction of excited spin-states even at 0 K. Estimations of the fraction of excited spin-states needed to obtain the observed levels of magnetization seem to definitively favor a HS interpretation in the thin films,[96, 97] and a HS state in strained thin-films has also been obtained from first-principle calculations.[95]

The HS character is closely connected to substrate induced strain and thus the lattice parameters but in exactly which way is not understood. Interestingly, epitaxial thin films of LaCoO<sub>3</sub> grown without strain exhibit some degree of magnetization while unstrained poly-crystalline thin films grown on Si substrates does not exhibit a FM HS ground state,[89, 92] suggesting that the epitaxial adhesion to the substrate plays a role.

The interplay between the spin-state and lattice parameters in LaCoO<sub>3</sub> has been discussed since Goodenough realized that the ionic size difference between the small LS and large HS Co<sup>3+</sup> ions can stabilize a 1:1 LS-HS ratio in a checkerboard pattern.[2, 73] Within this scenario, cooperative lattice effects inhibit HS-HS nearest neighbours and "repulses" the HS sites from each other. It has also been suggested that lattice relaxations are the cause for the reduced spin-gap, which without lattice effects have been estimated to  $\sim 50$  meV.[83, 85] Further, ultrasonic measurements have observed anomalous lattice softenings and lattice expansions that coincide with the spin-state transitions.[98]

With the wealth of experimental data available it seems clear that the spin-state transitions in LaCoO<sub>3</sub> occur with significant influence from the lattice, including the Co-O distance  $r$  and Co-O-Co angle  $\omega$ . This can be seen in Fig. 3.5 which displays the estimated LS fraction as a function of temperature given

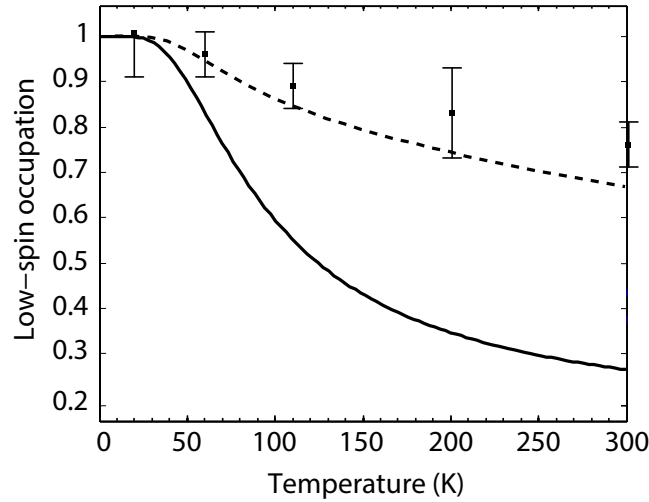


Figure 3.5: Low-spin fraction as a function of temperature. The squares with errorbars were obtained from X-ray absorption on the Co- $L_{2,3}$  edge, the dashed line is the prediction from thermodynamical data. and the solid line is the Fermi occupation Eq. 3.3 with  $Z = 5$  and  $\Delta = 200$  K.

by (1) XAS together with configuration interaction multiplet calculations[83] (squares with errorbars), (2) Magnetic susceptibility and heat capacity together with thermodynamic theory[85] (dashed line), and (3) Fermi statistics with  $\Delta = 200$  K (solid line).

It is clearly seen that the experimental LS fraction increases more slowly and deviates considerably from the simple thermal occupation, implying a mechanism that inhibits the LS depopulation. Note that there is no physically sound combination of  $Z$  and  $\Delta$  that manages to capture the experimental data.

Several suggestions for such mechanisms have been proposed,[74, 83, 85] for example a "negative cooperativity"[86] where  $\Delta = f(n_{HS})$  increases with the population  $n_{HS}$  of the HS state. Fundamentally though, it should be expected that a valid mechanism will be based on the interplay between the lattice and Co spin-state. Here, experiments on strained thin-films have the possibility to give unique insights. The effect of tensile epitaxial strain[92] (increased HS character) has been shown to be, in some respects, opposite to the effects of hydrostatic and chemical pressure[74] (decreased HS character), as is expected if one considers, somewhat naively, that the larger HS  $\text{Co}^{3+}$  ion becomes more energetically favored when the lattice parameters and unit cell volume increases.

Consider in this regard an isolated  $\text{CoO}_6$  cluster and the variation of spin-gap with  $r$  and  $\omega$ . The intraionic exchange energy  $\Delta_{\text{ex}}$  is practically constant for a given ionic species and does not depend on the lattice environment, while  $\Delta_{\text{CF}} \sim r^{-5}$  and  $W \sim \cos(\omega)r^{-3.5}$ . [74, 90] With these relations in mind, the naive assertion above can be somewhat justified. It is the reduction of  $\Delta$  through the strain induced changes in  $W$  and  $\Delta_{\text{CF}}$  that makes the magnetic HS

ground state possible in thin films. However, this approach neglects collective interactions outside the nearest neighbour approximation and does not explain the *constant* HS fraction observed in the thin films.[96, 97]

Part of the difficulty in assessing the nature of the excited spin state and its connection to the lattice properties stems partially from the lack of spin-state sensitive measurements. The reported spin-state fractions as a function of temperatures are all just estimations given by fitting or simulating a measured quantity, not explicitly related to the spin-state, to a model in which the spin states enter.

In principle, depending on the relative fraction of LS and HS sites, the dipole allowed  $p$ - $d$  transitions will differ in magnitude with varying spin-state. Sensitive optical measurements could then in principle be used to directly measure the variation of spin-state occupation with temperature. This fact is used in **Paper I**, where the first ultrafast pump-probe experiment on LaCoO<sub>3</sub> is presented.

Our results indicate that such measurements are indeed possible and show the existence of a lattice mediated "high-spin repulsion", responsible for the deviations from the thermal Fermi-statistic HS occupation. This repulsion is found to be only weakly temperature dependent which explains the constant HS fraction deduced from XAS measurements.[96, 97] From the observed sensitivity of the repulsion on the exact strain state it is possible that the adhesion to the substrate, and the resulting inhibition of the anomalous lattice expansion of LaCoO<sub>3</sub>, is responsible for the constant HS fraction in strained films. Without the high-spin repulsion, an even higher but non-constant HS fraction is to be expected, reflecting the thermal occupation according to Eq. 3.3.

Similar time-resolved measurements on bulk LaCoO<sub>3</sub>, in the presence of the anomalous lattice expansion and softening, could give an explicit measure of the magnitude of the lattice contribution to  $n_{HS}$ . In particular, the time-resolved result on the thin film suggests the following spin-state behavior in bulk LaCoO<sub>3</sub>: Starting with  $n_{LS} = 1$  at 0 K, a thermal HS occupation occurs until the saturation fraction imposed by the HSR is reached at  $\sim 50$  K.[86] At higher temperatures  $n_{HS}$  becomes constrained by the high-spin repulsion and the concept of a thermally activated  $n_{HS}$  is no longer useful. Additional HS occupation is achieved when the high-spin repulsion weakens as a consequence of the thermal lattice expansion and softening. The increased HS fraction will in turn effect the lattice in a feedback loop,[88] resulting in the anomalous lattice expansion.

This chain of arguments implies that a LaCoO<sub>3</sub> sample that is forced to keep the same lattice constants as the temperature is increased will not show the LS-HS transition. Indeed, a constant HS fraction, due to a combination of strain induced reduction of  $\Delta$  and epitaxial adhesion to the substrate, is observed in thin film samples and bulk LaCoO<sub>3</sub> under hydrostatic pressure consequently exhibits a pronounced LS character.[74]

Our interpretation is in some aspects similar to the proposed "negative co-

operativity” suggested by Kyômen *et al.*[85, 86], where the deviation from a purely thermally activated  $n_{HS}$  comes from an effective temperature dependence of  $\Delta$  through an  $n_{HS}$  dependent energy of mixing between HS and LS sites. The abrupt deviation from the thermally activated behavior at 110 K in the thin film is difficult to reconcile with a  $n_{HS}$  dependent energy of mixing, and instead it can be argued that  $n_{HS}$  becomes ”lattice activated” as the high spin repulsion weakens with increasing temperature.

### 3.4 Proton Conducting $\text{Ba}_2\text{In}_2\text{O}_5$

Proton conducting oxides have a potential in applications such as electrolytes in hydrogen separation membranes, hydrogen sensors, and intermediate temperature solid oxide fuel cells.[99, 100] Acceptor doping, for example  $\text{In}^{3+}$  substituted for  $\text{Zr}^{4+}$  in  $\text{BaZrO}_3$ , creates an oxygen-deficient structure, in which protons can be incorporated by hydration. At high temperatures ( $\gtrsim 300$  °C), the protons may jump from one oxygen to another followed by reorientational diffusion of the O-H group in between such jumps.

In contrast to the transition-metal ions discussed in the earlier sections of this chapter, the highest occupied orbitals of the post-transition metal  $\text{In}^{3+}$  ion consists of a fully occupied  $4d$  shell. Thus, while the  $\text{Mn}^{3+} t_{2g}^3 e_g^1$  configuration of the  $\text{LaMnO}_3$  perovskite gradually charge compensates towards  $\text{Mn}^{2+} t_{2g}^3$  upon aliovalent  $\text{Ca}^{2+}$  substitution on the  $\text{La}^{3+}$  site, similar compensation in the  $\text{In}^{3+} t_{2g}^6 e_g^4$  containing perovskite  $\text{LaInO}_3$  is not favorable. Instead, the stability of a full  $d$  shell leads to chemical compensation on the oxygen sites, reducing the oxygen content towards the brownmillerite  $A_2^{2+}\text{In}_2^{3+}\text{O}_5^{2-}$  composition. Such brownmillerites, exemplified in this section with  $\text{Ba}_2\text{In}_2\text{O}_5$ , consist solely of ions with fully occupied shells. The  $d$ -orbital effects that are the cause for many of the interesting properties of transition-metal perovskites are thus missing, making the oxygen vacancies the main source of interest in these and other related perovskite materials.

At low levels of atomic substitution the oxygen vacancies in the doped perovskites are randomly distributed amongst the oxygen octahedra. Instead, ordered oxygen vacancies are encountered at the other extreme, where the brownmillerite structure is realized. The brownmillerite structure can be regarded as an oxygen deficient perovskite structure where the ordered oxygen vacancies stabilize a layered structure with alternating oxygen octahedra and tetrahedra along the  $c$ -axis.

The brownmillerite crystalline structure of  $\text{Ba}_2\text{In}_2\text{O}_5$  consists of alternating layers of oxygen octahedra and tetrahedra, centered around the In atoms, see Fig. 3.6(a) where also the atomic site labeling is explained. The brownmillerite structure can adopt a number of different space group symmetries depending on the relative orientation of successive tetrahedral layer along the  $c$ -axis, where in each layer the tetrahedral tilt angle can be either  $\alpha$  (”left”, L) or  $-\alpha$  (”right”,

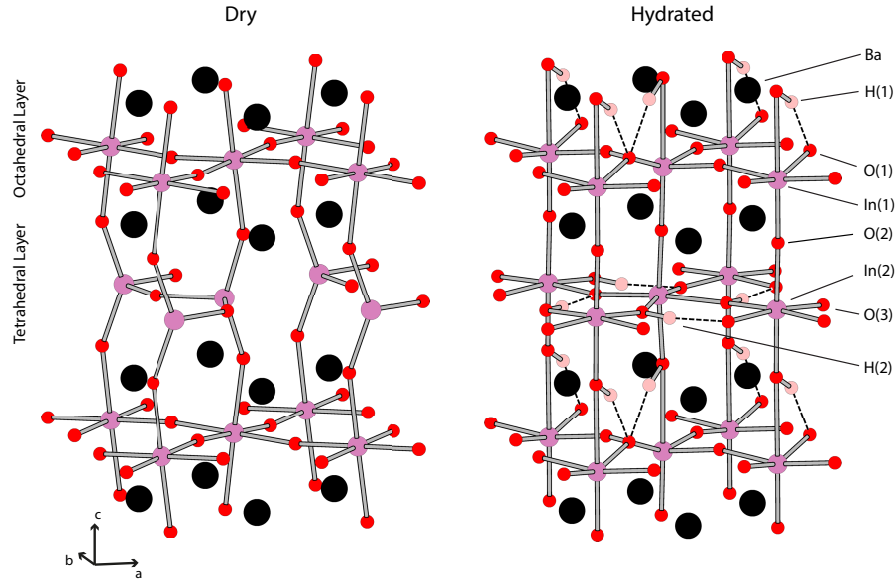


Figure 3.6: Left: The dry (dehydrated) brownmillerite structure of alternating InO<sub>6</sub> octahedra and InO<sub>4</sub> tetrahedra. Right: The hydrated structure as suggested by DFT calculations.[101]. The labeling of the atomic sites are explained to the far right of the figure.

R) with the most common being *Icmm* with random, *Ibm2* with the same (L, L, L,...), and *Pcmm* with alternating (L, R, L,...) orientation respectively.[102]

The hydrated phase, BaInO<sub>3</sub>H, shown Fig. 3.6(b), is obtained as the oxygen vacancies (V) are filled through the reaction



where  $\bullet$  indicates a positive charge relative to the O<sup>2-</sup> ion. Neglecting the protons, the crystal structure in the hydrated phase can be described as a layered perovskite structure, alternating between two different octahedra along the *c* direction, see Fig. 3.6(b). Superimposed on this structure, the incorporated protons induce significant local distortions depending on their spatial distribution. Both neutron diffraction[103] and DFT calculations[101] arrive at essentially the same point with a structure containing two proton sites. The H(1) protons are covalently bonded to the apical O(2) oxygens and form a hydrogen bond towards the one of the O(1) oxygens in the "octahedral layer". Within the "tetrahedral layer" the H(1) protons form both covalent and hydrogen bonds with O(3) oxygens.

However, the DFT calculations show small energy differences between different hydrogen bond orderings within the H(1) array, and what is shown in Fig. 3.6(b) is the lowest energy structure. The average structure obtained with diffraction techniques can be expected to be very similar independent of

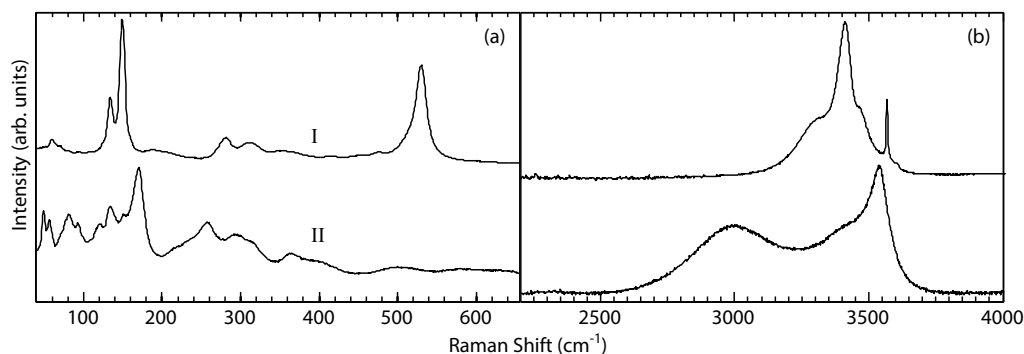


Figure 3.7: Raman spectra taken on two  $\text{BaInO}_3\text{H}$  samples. Phase I was obtained on a sample hydrated at both a longer time and at a higher temperature compared to the sample giving rise to phase II. The differences in both the (a) lattice and (b) OH-stretch modes indicate a structure in phase II associated with a more disordered proton arrangement as inferred from the much broader distribution of OH-stretch frequencies between  $2500\text{--}4000\text{ cm}^{-1}$  compared to phase I.

these local differences. In this respect, the sensitivity to small local distortions and differences in bond lengths, makes vibrational spectroscopy an excellent complement to diffraction.

To this date, even though both the structure and oxygen-proton vibrations are important for the proton transfer responsible for the proton conductivity,[104, 105, 106] there are very few studies on  $\text{Ba}_2\text{In}_2\text{O}_5$  that utilizes vibrational spectroscopy. In **Paper VI** the first attempt at providing an assignment of the Raman active phonons in  $\text{Ba}_2\text{In}_2\text{O}_5$  is presented. Based on this assignment, a temperature study is presented in **Paper V** in which the transition from the hydrated to the dry structure is investigated in detail.

In addition to the data presented in the two manuscripts, the spectroscopic investigations have shown evidence of two distinct local structures in the hydrated phase, seen in Fig. 3.7. A hydrated  $\text{Ba}_2\text{In}_2\text{O}_5$  sample is in general a mixture of the two phases and gives a Raman spectrum consisting of a linear combination of the two phases. A correlation between the local structure and hydration time/temperature as well as atomic substitution has been observed, with a phase I spectrum indicative of longer hydration times/higher temperatures, but a more systematic variation of sample preparation condition is needed to assert whether this is indeed the case.

If the observed correlation can be extended to a systematic transition between the two structures, one possible interpretation would be that the sample II spectrum belongs to a metastable structure reminiscent of the proton distribution right after their incorporation in the structure. After longer times or at higher temperatures, the protons have the possibility to reach the global minima in energy which would then correspond to the sample I structure.

The results presented in **Paper V** indicate that the proton arrangement in phase I is not compatible with calculations and diffraction data.[101, 103] In particular, calculations of the vibrational spectrum in the O-H stretch region predicts two distinct bands at  $\sim 2800$  and  $3300 \text{ cm}^{-1}$  respectively. These predictions are indeed closer to the phase II spectrum in Fig. 3.7, where two broad bands centered at  $3000$  and  $3500 \text{ cm}^{-1}$  are found. It is thus possible that the diffraction measurement from Jayaraman *et al.*[103], upon which the calculations by Martinez *et al.*[101] are based, was made on a sample in phase II.

### 3.5 Iron-Pnictide Superconductors

Since the discovery of high temperature superconductors, the cuprates, in 1986,[107, 108] understanding their unusual properties has been regarded as one of the most important questions by the condensed matter physics community. It is therefore no surprise that when Japanese scientists in 2008 discovered the second known class of high temperature superconductors,[109] the condensed matter community responded with huge enthusiasm. This second class of superconductors is based on iron and arsenide (or phosphor, both in the pnictogen group), compared to copper and oxygen in the cuprates, and is consequently known as either iron-arsenide or iron-pnictide superconductors. Common for the two classes of high temperature superconductors is that the Bardeen-Schrieffer-Cooper (BCS) theory fails completely to explain  $T_c$ , the temperature when superconductivity appears. Interestingly, both the cuprates and to a lesser extent the iron-pnictides consist of two dimensional layers in which the superconductivity is thought to occur.[110, 111]

The more pronounced two dimensionality in the cuprates might be one reason for the higher  $T_c$  compared to the iron-pnictides. To date, the highest  $T_c$  achieved by a cuprate is  $135\text{K}$  ( $\text{HgBa}_2\text{Ca}_2\text{Cu}_3\text{O}_x$ ),[112] while a more modest  $T_c$  of  $55\text{K}$  ( $\text{SmFeAsO}_{1-x}\text{F}_x$ ) has been reached by iron-pnictides.[113] Despite the comparatively low  $T_c$  in the iron-pnictides, the  $T_c$  is still large compared to traditional superconductors and as a completely new class of high temperature superconductors they might help pave the road towards an understanding of the ever so elusive cuprates.

#### Crystal Structure

Analogously to the oxygen-copper layers in the cuprates, all the iron arsenide superconductors have an approximately two dimensional iron-arsenide layer in common, in which superconductivity is thought to occur. This layer is built up of iron atoms surrounded by arsenide atoms in a tetrahedral arrangement[114, 115], see Fig. 3.8. In an exactly tetrahedral structure the As-Fe-As angle is equal to  $\arccos(-1/3) \sim 109.47^\circ$ , and it has been found that  $T_c$  has its

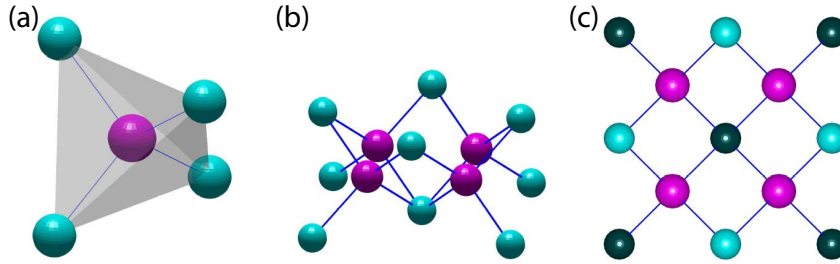


Figure 3.8: (a) The tetrahedral unit composed of the Fe atom (purple) surrounded by four As atoms (green) at the vertices of the tetrahedra. The quasi 2D Fe-As layer common for all iron-pnictide superconductors is shown in (b) and (c). In (c) the layer is viewed from straight above, with the darker As atoms lying below the Fe layer while the lighter As atoms lie above.

Table 3.2: Brief summary of the basic properties of the different classes of iron-pnictide superconductors.

Shorthand	Composition	Maximum $T_c$	a (Å)	c (Å)
1111	$ReFeAsO$	56K [113]	4 [114, 118]	8.5 [114, 118]
122	$AFe_2As_2$	38K [119]	3.9 [119]	13.2 [119]
111	$AlFeAs$	18K [120]	3.8 [120]	6.4 [120]
11	FeSe	15K [121]	3.7 [121]	5.5 [121]

maximum when this angle is close to ideal[116] although recent observations indicate this observation is not general for all types of iron-pnictides.[110]

Apart from the two dimensional Fe-As layers, different types of iron-pnictides have different amount of interspacing atoms. Depending of the structure of the interspacing layers, one finds four different classes of iron-pnictide superconductors [111, 117] which are summarized in Table I. The table includes shorthand names, composition ( $Re$  = rare earth,  $A$  = alkaline earth and  $Al$  = alkali metal), maximum  $T_c$  and the a- and c-axes for the four classes.

The difference between the four different classes is the amount of elements in the layers inbetween the Fe-As layers (FeSe in '11' compounds): In the '1111' compounds, the Fe-As layers are interspaced by  $ReO$  layers identical in structure to the Fe-As layers; in the '122' a layer of only  $A$  atoms lie inbetween; in the '111' compounds the larger  $Al$  atoms and in the '11' compounds the FeSe layers do not have anything separating them from each other.[111, 117] High Temperature Superconductivity is found in the '1111' and '122' structures, whose crystal structures are shown in Fig. 3.9.

### Mechanism behind and symmetry of the superconducting state

In the traditional BCS theory, superconductivity is due to electrons forming Cooper pairs through an electron-electron attraction caused by an overscreen-

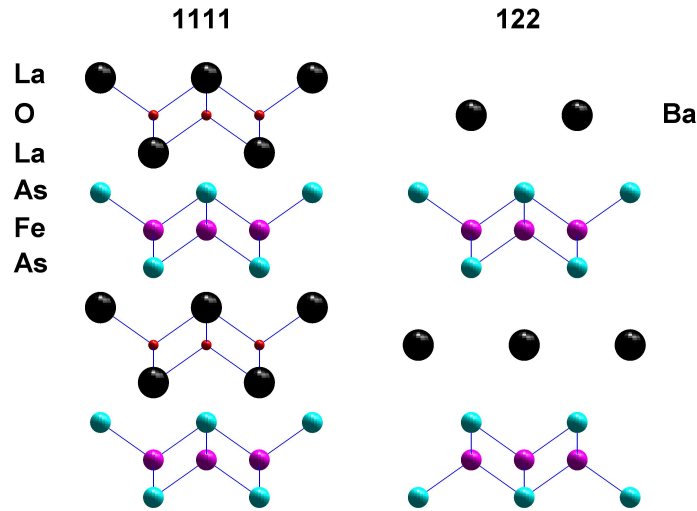


Figure 3.9: The crystal structures, viewed along the b-axis, of LaFeAsO of the '1111' family and BaFe<sub>2</sub>As<sub>2</sub> of the '122' family.

ing electron-phonon interaction.[122] Thus, a strong electron-phonon interaction involving high frequency phonons is needed if high transition temperatures are to be achieved.[123] It is generally believed that the electron-phonon coupling cannot be the glue that holds the cooper pairs together in cuprates, even though the electron-phonon coupling is rather strong.[123] In the iron-pnictides the electron phonon coupling is very weak, leading to estimates on  $T_c$  of the order of a few Kelvins, which makes the case for phonon mediated superconductivity improbable.[124]

A peculiar complication is found in the isotope effect, often mentioned as evidence for the electron-phonon mechanism for superconductivity, whereby  $T_c$  changes due to a shift in phonon frequencies because of the change of atomic masses.[125, 126] This effect is, rather surprisingly, large in the iron-pnictides, seemingly at odds with the small electron-phonon coupling observed.[127]

The temperature-doping phase diagram of a typical iron-pnictide can be seen in Fig. 3.10(a). The most interesting observation is the antiferromagnetic phase at low doping[128, 129], that disappears at the same time that superconductivity appears. In this diagram, the doping is induced by substituting the oxygen site with fluorine which injects electrons into the Fe-As layer although the Fe layer shows indications of being effectively hole doped.[130] Superconductivity can be induced also via doping by substituting any of the four comprising elements[109, 119, 131, 132], by oxygen deficiency[133] or by applying pressure.[134] Because the Fe atoms are what is thought to be responsible for the superconductivity, it is surprising that superconductivity can be induced by substituting the Fe site with Co. For example in the cuprates, substituting the Cu sites with Ni or Zn is an efficient way of destroying the

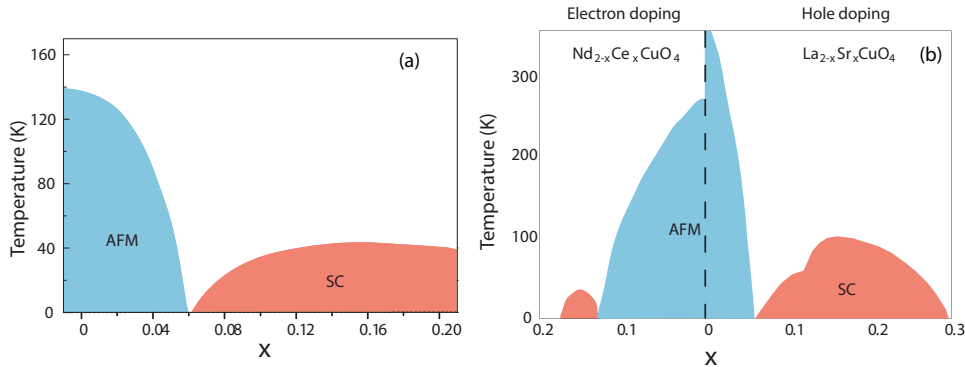


Figure 3.10: (a) Simplified phase diagram for  $\text{CeFeAsO}_{1-x}\text{F}_x$  as a function of temperature  $T$  and doping  $x$ . (b) Simplified general phase diagram for the high temperature superconducting cuprates. The x-axis shows the amount of doping, hole or electron, on the copper atoms. The appearance of superconductivity when the antiferromagnetic state disappears indicates a close relationship between these two states. Note the striking similarities between (a) and (b). (a) is adapted from Zhao *et al.*[115]. (b) is adapted from Bonn *et al.*[136].

superconducting state.[135]

The interplay between superconductivity and magnetism looks very similar to the case of the cuprates, see Fig. 3.10(b). This observation suggests that the superconductivity might be magnetically mediated and either cooperating or competing with the antiferromagnetic state, something that first-principle calculations predicted mere days after the discovery of high  $T$ -superconductivity in the iron-pnictides.[124] It seems that all the mentioned methods for achieving superconductivity works by suppressing the long-range magnetism encountered in the parent compounds, suggesting that the interplay between long-range magnetism and superconductivity is competitive.[110, 137]

These similarities between cuprates and iron-pnictides are paralleled by a number of differences. To begin with, the Fermi level in the cuprates can be modeled as being crossed by a single band while the iron-pnictides inherently are multiband in their nature; the Fermi level in the iron-pnictides is composed of the five  $3d$  orbitals from the iron atoms partly hybridized with the As  $4p$  orbital[138].

A defining characteristic for superconductors is the symmetry of the superconducting gap, which is related to the energy needed to break the cooper pairs.[123, 125] This symmetry gives the momentum dependence of this energy and in an ordinary BCS superconductors this symmetry is  $s$ -wave, meaning an isotropic gap with magnitude independent of the direction in momentum space. The high temperature cuprate superconductors on the other hand have a  $d$ -wave gap with four nodes along which the pair braking energy is zero.[139] Experimental and theoretical data suggest that the gap symmetry in the iron-

pnictides is isotropic, but of the more complicated  $s_{\pm}$ -wave type.[124, 140] The  $s_{\pm}$  superconducting state is characterized as a two gap state with a reversal of the phase of the order parameter between the two gaps. These two gaps are thought to originate from different bands visible as hole and electron pockets on the Fermi surface respectively, again accentuating the importance of multiband effects in the iron-pnictides.[124, 138] Calculations suggests that superconductivity is mediated by a magnetic excitation connecting the electron and hole pockets. In almost all superconducting iron-pnictides, neutron scattering measurements have found exactly such magnetic excitations with a wave vector connecting the electron and hole pockets,[128] in excellent agreement with the calculations mentioned above.[110] These results are consistent with the findings in **Paper VI**, where a combination of Raman spectroscopy and perturbative phonon-phonon calculations are used in order to investigate the phonon-phonon interaction via the anharmonic phonon decay.

So far, an unambiguous determination of the gap symmetry has not been found. It has been shown theoretically though, that the electronic Raman signal from a  $s_{\pm}$  superconductor shows distinct features that unambiguously could distinguish between a  $s_{\pm}$  gap and other gaps.[141] Unfortunately, the Raman cross section is very low in the iron-pnictides and the electronic background is yet to be observed and only very weak effects when crossing  $T_c$  has been found.[142, 143, 144, 145]



# 4

## Experimental Methods

### 4.1 Time Resolved Spectroscopy

The fundamental timescales in matter range from attoseconds (intra-atomic electron dynamics) up to minutes or even longer (glass transitions). In many regards however, the macroscopic properties of condensed matter systems depend on processes occurring on the femtosecond–picosecond timescale, including the interaction between different degrees of freedom. Such interactions are for example the electron-lattice couplings, electron-spin couplings and intersite electron-electron interactions. On a basic level, all of these interactions are mediated by the virtual exchange of electromagnetic quanta (photons) and the only direct way to influence them is thus via the electromagnetic field, i.e via light.

The possibility to directly perturb a material on the time-scale of the basic interactions presents many interesting opportunities from both a fundamental and applied point of view. Such perturbations, and the subsequent measurements of the induced effects, are carried out with the use of very short laser pulses and constitutes the principle for the plethora of time resolved spectroscopy techniques available today. In general, the perturbation arise from the dipole allowed absorption and subsequent energy transfer within the sample. Ultrashort laser pulses routinely carry a peak power in the gigawatt range and the number of photons is comparable to the number of unit cells in the interaction volume, implying that the number of absorbed photons per unit cell can be close to unity. As a consequence, the sample can be driven by photon absorption into a regime where its properties are distinct from those at any point in the equilibrium phase space. However, such drastic deviations from equilibrium are not always desired and in such cases the laser pulse is attenuated as to create a photoexcited state describable in terms of an expansion around the steady-state parameters.

Both the high-fluence and low-fluence regimes described above are of scientific interest. The aim of high-fluence investigations[146] can be for example to study phase transitions[147, 148], melting[149, 150] or to reach otherwise unattainable phase-space points[151, 152], and is of both applied and fundamental interest. Low-fluence experiments are of more fundamental interest and have provided important insights into for example the Cooper-pair formation[153] and quasi-particle recombination[154] in superconductors.

In the following sections, photoinduced dynamics and some experimental considerations underlying time-resolved spectroscopy will be explained in more detail. First, general aspects of non-linear optics will be described with a focus on effects that are used in ultrafast instrumentation. The general principles of pump-probe experiments is explained, and finally an account of the light-matter interaction and ensuing dynamics on the femtosecond timescale is presented.

### 4.1.1 Introduction to Ultrafast Optics

The very short duration of the laser pulses in a time-resolved experiment leads to additional considerations as compared to experiments carried out with ordinary continuous wave (CW) lasers. Due to the uncertainty principle, laser pulses with a finite length invariably contain a continuous range of frequencies and care must be taken to ensure identical propagation of all frequencies in the pulse.

Apart from negative complications, the high photon density in ultra-short laser pulses also allows for advantageous non-linear effects which can be used to shape the pulse in the time, frequency and spatial dimensions, thus adding to the experimental flexibility when working with pulsed lasers.

In the following, these and similar effects will be discussed in more detail.

#### Ultrashort Laser Pulses

The most obvious characteristics of a laser pulse is its temporal duration, amplitude and wavelength. Apart from these properties, there are several additional properties needed to fully characterize the pulse, properties that are more readily seen in frequency space. Amongst these additional properties the most important are the energy spread and the so called chirp.

An ordinary laser consists of a resonant cavity and the sharp monochromaticity is due to that only certain very well defined frequencies can be supported as standing waves inside the gain envelope of the lasing media.[155] Short laser pulses on the other hand must give up monochromaticity due to Heisenbergs uncertainty principle which states that a laser pulse with temporal duration  $\tau$  must obey [156]

$$\tau \cdot \Delta\nu \geq K, \quad (4.1)$$

where  $\Delta\nu$  is the frequency spread of the pulse and  $K$  is a constant that depends on the pulse shape. Moreover, it is easy to show that the minimum spread

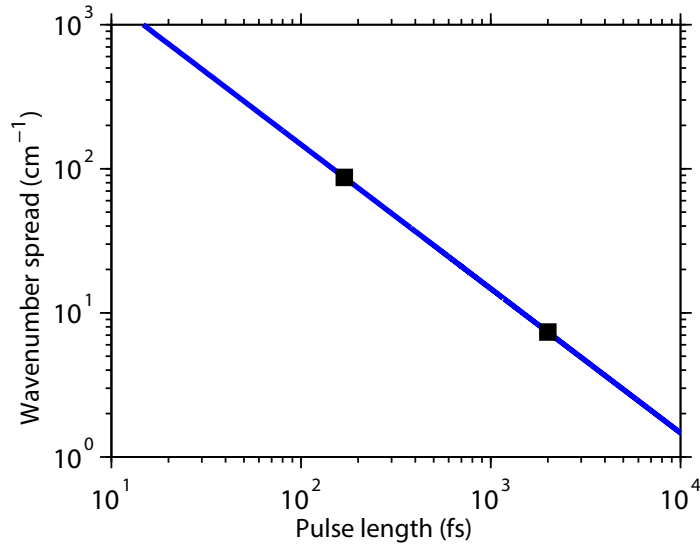


Figure 4.1: Spread in wavenumbers as a function of pulse duration. The squares indicate the pulse lengths, 150 fs and 2 ps, available in our experimental setup.

in wavelength  $\Delta\lambda$  and wavenumber  $\Delta\tilde{\nu}$  are  $\Delta\lambda_{min} = K\lambda^27(c\tau)$ , and  $\Delta\tilde{\nu}_{min} = K/(100c\tau)$  respectively, where  $c$  is the speed of light,  $\lambda$  is the central wavelength of the pulse and  $\tilde{\nu}$  is measured in inverse centimeters. The smallest theoretical value of  $K$  is obtained for a perfectly Gaussian pulse where it take the value  $1/2$ , while other pulse shapes give inequalities with a right hand side larger than  $1/2$ .

The energy spread defines the energy resolution in our experiments and is illustrated in Fig. 4.1 where the minimum spread is given as a function of pulse duration.

A pulse obeying Eq. (4.1) is called transform limited and is the ideal working condition. Ultrashort pulses are very "fragile" and a transform limited pulse is very easy to destroy.[157] Imagine for example a pulse travelling through a glass plate. For glasses, the refractive index  $n$  generally varies as  $1/(n^2 - 1) \sim \lambda^{-2}$  in the region of visible light.[158] The (effective) speed of light is modified by the refractive index,  $v = c/n$ . Thus, blue light will travel slower than red light through an ordinary glass plate. Because ultrashort pulses contain a range of wavelengths, the redder wavelength will become separated from the bluer as a consequence. The frequency content of the pulse will not change but it will become extended in time, the pulse is *chirped* as is illustrated in Fig. 4.2. The chirp feature has negative effects on the temporal resolution and generation of coherent effects.

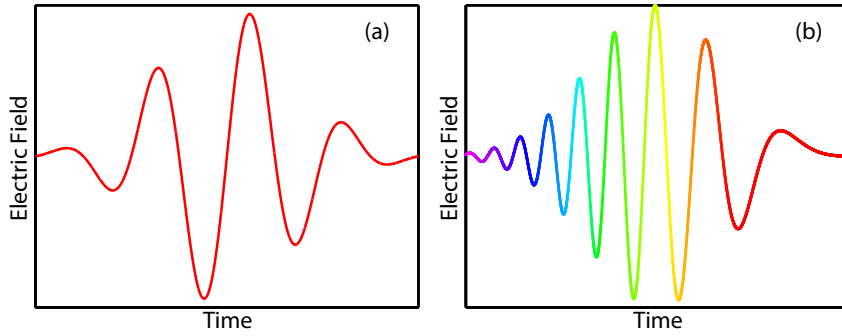


Figure 4.2: (a) Electric field versus time for a diffraction limited pulse with Gaussian envelope. (b) Electric field versus time for a chirped pulse. A chirped pulse always has  $\tau \cdot \Delta\nu$  larger than the transform limit in Eq. (4.1). The color is proportional to the instantaneous frequency (blue = high frequency, red = low frequency).

### Non-Linear Optics

A femtosecond laser typically produces a mean power in the Watt range, comparable to typical power levels in CW lasers used for spectroscopy. This power is distributed over the time that the pulses occupy as well as the time without pulses. The laser used in the work presented in this thesis produces 150 fs pulses with a repetition frequency of 1 kHz, implying that each second only contains 150 ps of photons. The average power in each pulse will therefore be  $1/150 \cdot 10^{12}$  W which is in the order of gigawatts, billions of times higher than the average power. With such extremely high instantaneous power, non-linear effects in the photon-matter interaction become important.

In the classical approach the response of matter subjected to an electric field  $E$  is given by the electric polarization  $P$ , defined as [158]

$$P(\omega) = \chi(\omega)E(\omega), \quad (4.2)$$

with  $\chi$  the electric susceptibility. The frequency content of  $P$ , the frequencies radiated back by the irradiated matter, will in this case be the same as in  $E$  and the frequency dependence of  $\chi$  determines the magnitude of  $P$ . Eq. 4.2 can be viewed as the first term in a Taylor expansion of a more general relation between  $P$  and  $E$  where higher powers of  $E$  also play a role. In most cases the  $E$  field from the light is relatively small so that only the linear term contributes. However, when the density of photons (and hence power) is sufficiently high the terms quadratic and even cubic in  $E$  become noticeable. The presence of these higher order terms drastically changes the response to the light and gives rise to several non-linear optical effects. Including higher order terms,

$$P = \chi E + \chi_2 E^2 + \chi_3 E^3 + \dots \quad (4.3)$$

It is instructive to rewrite Eq. (4.3) by factoring out  $E$ ,

$$P = [\chi + \chi_2 E + \chi_3 E^2 + \dots] E, \quad (4.4)$$

so that an effective, E-field dependent susceptibility  $[\chi + \chi_2 E + \chi_3 E^2 + \dots]$  is introduced. From  $P$  it is possible to obtain, via the susceptibility, the dielectric constant and hence also the complex index of refraction. Because the susceptibility now depend on the E-field, it follows that the optical properties also depends on the E-field. In other words, light with very high intensity alters temporarily the material it travels through, creating an intensity dependent non-linear optical response.[156]

As an example, in materials where the refractive index increases with the intensity of light, high intensity light will experience an effective positive lens effect that focuses the intense light, creating even more intense light that again is focused even more. This process, self-focusing, continues until the material is saturated and is an important step in the creation of stable ultrashort pulses.[156, 157]

## Second Harmonic Generation

One of the simplest and most commonly used non-linear effects is frequency conversion, where the frequency of the re-irradiated light is modified by the interaction with matter. A simplified explanation of this effect takes into account the quadratic term in the expansion 4.3 and assumes a harmonically oscillating electric field  $E = E_0 \sin \omega t$ .

The induced electrical polarization, given by  $P$ , in the material is in this case

$$P = \chi E_0 \sin \omega t + \frac{1}{2} \chi_2 (1 - \cos 2\omega t). \quad (4.5)$$

The second term, arising from  $E^2$ , gives rise to a response with double the frequency of the driving  $E$  field.[159] This phenomenon is called second harmonic generation (SHG) and is important in many laser applications.

## Frequency Mixing

If the electric field only contains one frequency component, SHG is the only possible non-linear effect. With two frequency components present, as is the case for example when two different laser beams intersect inside the non-linear medium, the optical response becomes more complicated:

$$P = \chi E + \chi_2 [E_1^2 (1 - \cos 2\omega_1 t) + E_2^2 (1 - \cos 2\omega_2 t) + \quad (4.6)$$

$$+ E_1 E_2 (\cos (\omega_1 - \omega_2)t - \cos (\omega_1 + \omega_2)t)]. \quad (4.7)$$

In addition of SHG of the two frequencies  $\omega_1$  and  $\omega_2$ , new *frequency mixing* components  $\omega_1 - \omega_2$  and  $\omega_1 + \omega_2$  arise from the frequency difference and frequency

sum.[159] This effect forms the basis of the optical parametric amplification described in detail below.

### Conditions for Achieving Non-Linear Effects

In the above sections non-linear effects have been treated in a highly simplified manner. In practice though there are several conditions besides the high intensity that must be fulfilled in order for the non-linear effects to be observable.

To start with, properties arising from the quadratic term  $\chi_2 E^2$ , i.e SHG, can only be observed in materials without an inversion symmetry. A material with inversion symmetry is characterized by that the properties at point  $\mathbf{r}$  are the same as those at point  $-\mathbf{r}$ . That an inversion symmetry prohibits SHG can be understood by considering the fact that going from  $\mathbf{r}$  to  $-\mathbf{r}$  is equivalent to staying at  $\mathbf{r}$  and changing the sign of vector quantities. Applying this to  $P$  gives  $P(E) = -P(-E)$  because both  $P$  and  $E$  are vectors, leading to  $\chi_2 E^2 = -\chi_2 (-E)^2$ . This implies  $\chi_2 = 0$  and no quadratic non-linear effects are thus possible.[159]

Crystals without inversion symmetry are easy to find, a more important obstacle to high efficiency of the SHG and frequency mixing is phase matching. The discussion that follows uses SHG as a concrete example, but the case with frequency mixing is completely analogous. Intense light with frequency  $\omega$  continuously creates light at the second harmonic frequency  $2\omega$  as it travels through the medium. The refractive index,  $n$ , is in general frequency dependent, so that the speed of  $\omega$  and  $2\omega$  light is different. SHG photons created at different depth in a crystal might therefore interfere destructively, drastically decreasing the output intensity. It can be shown that the intensity  $I(2\omega)$  of the SHG is [156]

$$I \sim \left( \frac{\sin \Delta k l / 2}{\Delta k l / 2} \right)^2 \quad (4.8)$$

where  $l$  is the length traveled inside the non-linear medium and  $\Delta k = n_{2\omega} 2\omega / c - 2n_\omega \omega / c$ . To obtain the highest SHG power, the crystal must have the same refractive index at  $\omega$  as at  $2\omega$ . For the more general case of frequency mixing, the condition is  $n_{\omega_3} \omega_3 = n_{\omega_2} \omega_2 + n_{\omega_1} \omega_1$ , which reduces to  $n_\omega = n_{2\omega}$  in the special case of SHG. Fulfilling this condition is indeed very rare if  $\omega$  and  $2\omega$  have the same polarization. Fortunately, SHG often creates  $2\omega$  photons with a polarization perpendicular to the  $\omega$  photons (so called type I SHG). It is thus possible to use birefringent crystals, i.e crystals with different dispersions for the different polarizations. Due to the phase matching condition only a narrow frequency range is possible, but because the refractive index changes when the crystal is rotated, it possible to extend the working range immensely. At our laboratory we use a combination of  $\beta$  - BBO and LBO crystals, which can be rotated to create light in the range 550 nm-13  $\mu$ m by SHG and frequency mixing, see section 4.1.2.

### Determining the Length of Ultrashort Laser Pulses

In the previous sections (4.1.1 and 4.1.1), examples of the distinct properties of ultrashort laser pulses were discussed. This section describes different ways of characterizing these properties with an emphasis on the methods used at the time-resolved lab used in the work presented in this thesis.

Measuring the pulse duration is obviously of paramount importance when doing time resolved experiments. Realtime detectors are usually orders of magnitudes too slow for monitoring femtosecond pulses, they can only detect the integrated intensity of the whole pulse. With streak cameras it is possible to obtain a time resolution of the order 100 fs,[160] but even this is too slow for accurately determining the pulse intensity as a function of time for femtosecond pulses. There exists however, methods for detecting the average intensity profile of the emitted pulses.

The most common way of doing this, which is also used in the experiments presented in this thesis, is to use autocorrelation techniques.[157] The pulses whose duration is to be determined is split into two beams by a beam splitter, one of the pulses passing through a moveable delay. The two beams are then sent through a non-linear crystal where they are made to interfere with each other. When the pulses overlap, SHG is produced in the direction selected by the momentum conservation  $k_{SHG} = \vec{k}_1 + \vec{k}_2$ , with intensity proportional to the autocorrelation. Scanning  $\tau$  (i.e moving the delay), one obtains a signal that is the pulse profile convoluted with itself. As a simple example, assume a Gaussian pulse  $I(t) = I_0 e^{-(t/t_0)^2}$ , with a FWHM of  $t = t_0 \sqrt{\ln 2}$ . The autocorrelation is given by  $S(\tau) \sim e^{-(\tau/(2t_0))^2}$  with FWHM at  $\tau = t_0 \sqrt{2 \ln 2}$ , i.e a Gaussian that appears a factor of  $\sqrt{2}$  longer than the real pulse  $I(t)$ . This can be generalized to different pulse shapes, and independent of pulse shape the observed duration in the autocorrelation will appear longer than the real duration, but the amount varies with pulse shape.

However, the scheme explained above can sometimes give a misleading picture of the pulse shape as only the intensity is obtained. More advanced techniques rely on interferometric effects and capture also the phase information in the pulse.

#### 4.1.2 Pump-Probe Spectroscopy

The common principle amongst the different pump-probe techniques is to use the time resolution of the ultrashort pulses to initiate an excitation from the ground state up to a higher energy state and then follow the subsequent relaxation back to the ground state. This scheme requires two sets of pulses, the pump and the probe. The pump beam is responsible for initiating the excitation and the moment in time that the peak of the pump pulse hits the sample defines a zero time  $t = 0$ . After a variable time  $\Delta t$  the probe pulse is made to hit the sample at the exact same position as the pump pulse. Now, if  $\Delta t$

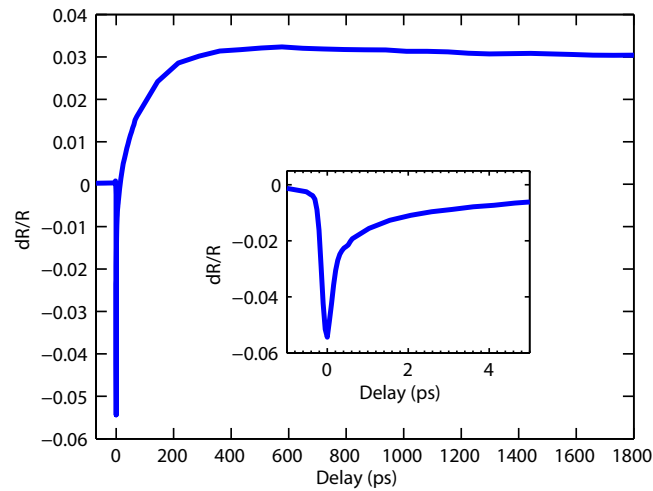


Figure 4.3: A typical transient as a function of delay between pump and probe. As the delay is scanned, the difference in reflected intensity due to the pump at  $t = 0$  is measured. Three distinct features can be seen: A zero signal at negative delays, indicating that the sample is in equilibrium before the pump arrives, a sharp peak corresponding to the immediate response to the pump, and finally the dynamical processes involved in the relaxation back to the equilibrium state. The inset shows a magnification of the features around the sharp peak close to  $t = 0$ . The data in this transient is taken on  $\text{LaMnO}_3$  at temperature 80K, far below the Néel temperature 156 K.

is not too large, the optical response of the sample will in general be different compared to if the pump was absent at time  $t = 0$ .

In a pump-probe experiment the difference in the probe pulse response with and without the pump pulse is measured and a typical experiment is performed by scanning the delay  $\Delta t$  over a set of times, ranging from some negative time to some positive time, while recording the change in probe pulse response for each time. The visualization of such a recording is called a transient, and an example can be seen in Fig. 4.3. In this case the delay ranges from -70 ps to 1800 ps, the time resolution is  $< 200$  fs, and the measured quantity is the change in reflectivity due to the pump beam.

### Experimental Setup

There are many variants of the pump-probe setup, most of them differing in what property of the probe pulse is being detected. The simplest pump-probe setup is when reflectivity is measured, as in Fig. 4.3. In that case it is only the intensity modulation of the probe, with and without the pump pulse, which is recorded but regardless of operating mode the general experimental setup is quite similar to the schematic shown in Fig. 4.4. The specifications in the schematic are taken from the setup used in the research presented in this thesis.

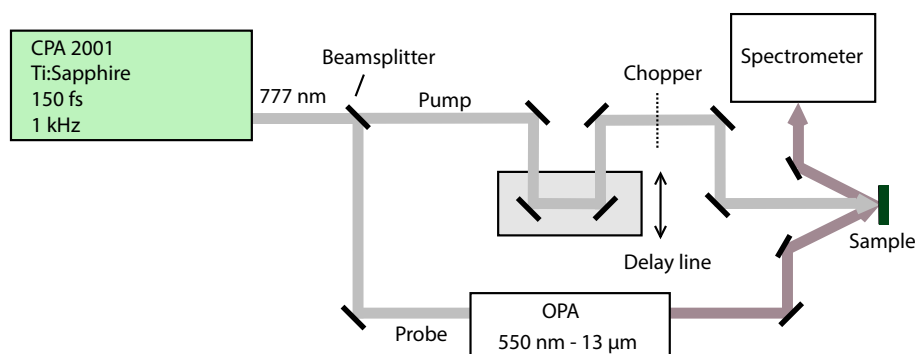


Figure 4.4: Schematic layout of the pump-probe setup used for the work in this thesis.

In the laser experimental scheme in Fig. 4.4 the laser is depicted in the upper left corner. The most important specifications of the laser are the central wavelength (also called fundamental of the laser), pulse duration and repetition frequency, which in this case are 775 nm, 150 fs and 1 kHz respectively. The repetition frequency states the number of pulses emitted each second and usually ranges between 1 kHz and 80 MHz. A high repetition frequency implies more pump/probe pulse pairs but with weaker peak power, and accordingly better statistics, less noise but also lower signals in the transient. On the other hand, the time between two subsequent pulses becomes quite short (12.5 ns for 80 MHz) so that some samples might not relax back to the ground state before the next pulse arrives. The average power emitted by the laser will in general not depend very strongly on the repetition frequency, and a laser with low repetition frequency will thus have more energy in each pulse, which can be crucial in high-fluency applications.

### Pump Beam

The upper beam in Fig. 4.4, which is normally used as the pump, is directed to the sample via a delay line and a chopper. By moving the delay line back and forth, the time  $\Delta t$  between the two pulses can be adjusted with an accuracy of a few femtoseconds. The chopper alternates between blocking and letting through the pump, either mechanically or by electro-optics, creating a probe signal modulated by the chopping frequency which can then be detected with a lock-in amplifier.

### Probe Beam and Continuous Frequency Tuning

The lower beam in Fig. 4.4 depicts the probe. Before arriving at the sample, this beam can be sent through a "TOPAS" optical parametric amplifier (OPA) which tunes the energy of the laser by using non-linear crystals, made from  $\beta - \text{BaB}_2\text{O}_4$  (BBO). The energy can be tuned continuously, resulting in output

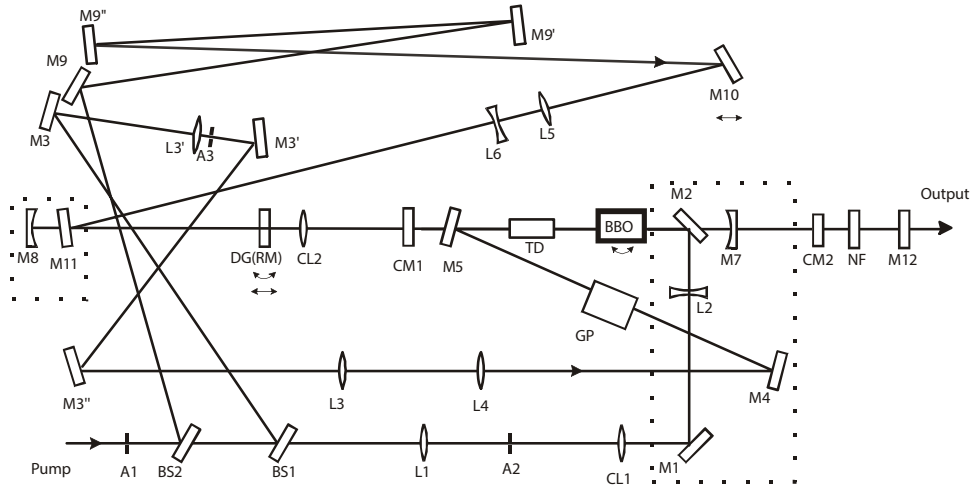


Figure 4.5: Schematic illustration of the OPA "TOPAS", [161] where two sets of pulses, centered around  $\omega_2$  (signal) and  $\omega_3 = \omega_1 - \omega_2$  (idler) respectively, are produced as output. See text for details. M = Mirror, L = Lens, CM = Cylindrical Mirror, CL = Cylindrical Lens, BS = Beam Splitter, TD = Time Delay, DG = Diffraction grating, A = Aperture, NF = 775 nm Notch Filter.

with a wavelength (energy) between 550 nm and 13  $\mu\text{m}$  (0.095 - 2.25 eV ), or expressed in wavenumbers, 770 to 18182  $\text{cm}^{-1}$ , i.e from the mid infrared to the visible. In order to achieve this broad range of possible emissions, a two-stage setup is used.

In the first stage, schematically shown in Fig. 4.5, the fundamental of the laser is split into three beams. The weaker of the beams passes through the two beam splitters BS1 and BS2 and creates the seed pulse via broad-band superfluorescent continuum generation in the BBO crystal, from which a narrow part centered at  $\omega_2$  is picked out by the diffraction grating (DG). This process requires three passes through the BBO crystal. In the fourth pass, the seed and the first (weaker) pump, reflected at BS1, intersects in the BBO crystal to shape the seed into a close to transform-limited pulse. The major part of the pump, reflected at BS2, intersects with the seed inside the BBO crystal in the final and fifth pass where the final amplification occurs. In the end, two pulses, centered around  $\omega_2$  (signal) and  $\omega_3 = \omega_1 - \omega_2$  (idler) respectively have been created at the expense of the pump at frequency  $\omega_1$ .  $\omega_1$  and  $\omega_2$  can be tuned continuously by rotating the BBO crystal and the diffraction grating DG.

The wavelength of the signal and idler beams generated in this way can be tuned between 1080–1560 nm and 1536–2731 nm respectively. To cover the whole range between 550 nm–13  $\mu\text{m}$ , either a second harmonic generation (SHG) or a difference frequency generation (DFG) stage can be used. The SHG stage uses an additional BBO crystal to produce light with wavelengths between 540–1415 nm. The DFG can be viewed as a "reverse" parametric am-

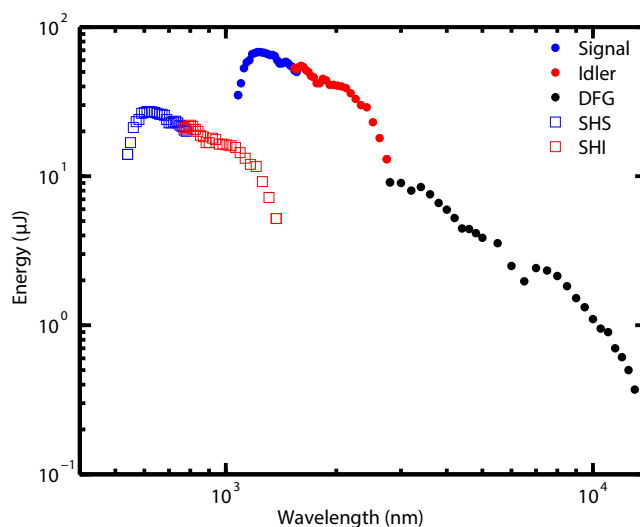


Figure 4.6: Benchmark pulse energies as a function of wavelength. DFG = Difference Frequency Generation, SHS = Second Harmonic of Signal, SHI = Second Harmonic of Idler. The SHG values are estimated from an assumed 20% conversion efficiency.

plification that uses an IR transparent crystal to produce wavelengths ranging from 2600–13000 nm. When reaching the limits of the possible wavelengths, the energy in each pulse as well as the intensity stability between pulses drops. Pulse energy as a function of wavelength in the setup is shown in Fig. 4.6.

### Spatial/Temporal Overlap

The pump and probe beams must overlap in both time and space at the sample position. A quick way of achieving good overlap is to use a BBO crystal and for example a manganite thin film. The manganite films are suitable as they give a strong transient response ( $<1\%$  with  $1 \text{ mJ/cm}^2$  excitation fluence) within the 2 ns delays that can be covered by the delay line, see Fig. 4.3. Inserting such a thin film at the sample position, it is thus possible to achieve spatial overlap by maximizing the observed transient signal, without worrying much about the temporal overlap. After the spatial overlap has been optimized, a rough temporal overlap can be obtained by finding the peak close to zero delay. At this stage, the BBO should be inserted instead of the manganite at the sample position. As described above, the BBO crystal is good for achieving frequency mixing and this occurs, without delay, when the pump and probe overlaps in time. Maximizing the frequency mixed output, one is sure that the pump and probe overlaps in both space and time.

### 4.1.3 Femtosecond Dynamics

This section will cover the physics behind the dynamics probed in time resolved spectroscopy. The focus will be mostly on the phenomenology in crystalline materials, which differs in some important aspect from liquids and gases. In the latter cases the relatively weak interatomic forces imply that orientational and vibrational motions of the molecules are important at short time scales.[157] Ultrafast dynamics in solid matter on the other hand is on a fundamental level expressed in terms of the electronic degree of freedom, with atomic (phonons) and spin excitations arising through energy transfer from the electronic system.[162, 163] A general account of the photoinduced dynamics represents a time evolution of the complete crystal Hamiltonian coupled to an electromagnetic source term representing the pump pulse. As always, such an approach is completely intractable. Different approximation schemes exist based on the timescales, measurement methods and if coherent effects are important or not. However, the hierarchy of processes and time-scales are to a large degree common to most solid state materials. The different dynamical steps in the relaxation of solid state materials is briefly described below. Later, the reason for these steps to be visible in optical experiments are discussed.

Photoexcitation is, on the time-scales accessible with laser-pulses, an instantaneous process that occurs during the whole duration of the pump pulse. The direct result of the pump-pulse excitation is the creation of electron-hole pairs and a corresponding non-thermal distribution of electrons in the conduction band<sup>1</sup>. Scattering between the excited carriers rapidly ( $\leq 100$ fs) equilibrate, while conserving their total energy, the electronic momenta to form a Fermi distribution centered at an elevated temperature.[146, 162, 164]

The electron system at elevated temperature contains an excess of energy that is dissipated by the release of phonons (electron-lattice coupling) or magnons (electron-spin and lattice-spin coupling). These processes are considerably slower than the electron thermalization time. Consequently, the release of phonons and magnons does not push the electronic subsystem out of the thermal Fermi distribution but rather lowers its temperature. Thus, it is justifiable to describe the subsystems with the so called three temperature model, in which separate electron ( $T_e$ ), lattice ( $T_l$ ) and spin ( $T_s$ ) temperatures are defined in addition to the number of non-thermalized excited carriers  $N$ .

Before the pump pulse  $I(t)$  all three temperatures are equal,  $T_e = T_l = T_s = T_0$ , but after the excitation they evolve separately until they reach a new equilibrium at a higher temperature  $T_1$ . At this point, the sample relaxes back to the ground state via heat diffusion and electron-hole recombination processes. The time evolution of these temperatures are quantified by a set of

---

<sup>1</sup>Here it is assumed that the pump wavelength is small enough for the excitation photons to traverse the energy gap between the highest occupied and lowest unoccupied band.

coupled differential equations[165, 166]:

$$\begin{aligned}
dN/dt &= -N/\tau_N + I(t) \\
C_e dT_e/dt &= -G_{el} \cdot (T_e - T_l) + \alpha N \\
C_l dT_l/dt &= -G_{le} \cdot (T_l - T_e) - G_{ls} \cdot (T_l - T_s) \\
C_s dT_s/dt &= -G_{ls} \cdot (T_s - T_l),
\end{aligned} \tag{4.9}$$

where the coefficients  $C$  denote the specific heats of the subsystems,  $G$  are the interaction constants between pairs of subsystems and the electron temperature is assumed to rise proportionally to the number of non-thermal excited carriers  $N$ . It has been observed experimentally that the timescales on which the different temperatures evolve decouple.[165] In this approximation the time evolution, with a Gaussian source term  $I(t) \sim \exp(-t^2/2\tau_I^2)$ , reduces to a sum of exponential rises and decays:

$$\begin{aligned}
N &= A_N \operatorname{erfc} \left( \frac{\tau_I}{\sqrt{2}\tau_{th}} - \frac{t}{\sqrt{2}\tau_I} \right) e^{-t/\tau_{th}} \\
T_e - T_0 &= A_e \left( \operatorname{erfc} \left( \frac{\tau_I}{\sqrt{2}\tau_{el}} - \frac{t}{\sqrt{2}\tau_I} \right) e^{-t/\tau_{el}} - N \right) + B_e \\
T_l - T_0 &= A_l (1 - e^{-t/\tau_{el}}) e^{-t/\tau_{ls}} + B_l \\
T_s - T_0 &= A_s (1 - e^{-t/\tau_{ls}}),
\end{aligned} \tag{4.10}$$

where  $\operatorname{erfc}$  is the complementary error function and the  $B$  constants reflect the fact that not all the excess energy is transferred. The time constants  $\tau$  orders as  $\tau_{th} \ll \tau_{el} \ll \tau_{ls}$  and describes the rate of electron-electron thermalization ( $\tau_{th}$ ), electron-lattice relaxation ( $\tau_{el}$ ), and lattice-spin relaxation ( $\tau_{ls}$ ).

The three-temperature model is only an approximation but often provides a good fit to measured data at times longer than picoseconds. In Fig. 4.7 the ultrafast response with a 25 fs time-resolution of (a) silver[168] and (b) silicon[167] are shown in order to highlight the limitations of the three-temperature model. Exciting intraband transitions within the conduction band, the electron-electron thermalization time was found to be close to the ps scale in gold and silver as a consequence of the large quasiparticle lifetime close to the Fermi energy.[166, 168, 169] Nevertheless, the rate-equation model, Eq. 4.10, provides an excellent fit (shown with a dashed line in Fig. 4.7(a)) to the data.

Silicon exhibits more complicated femtosecond dynamics, see Fig. 4.7. Besides the dynamical contribution from the excited electrons in terms of the free carrier (FC) and state-filling (SF) contributions, it is necessary to include coherent effects to fully describe the response to the excitation. Coherent effects arises from the fact that the photons in the excitation pulse impart their phase information in the excited carriers and last  $\leq 100$  fs, until the phase memory is lost due to the decoherent nature of the carrier-carrier scattering.[146, 162, 164, 167, 170] Besides the inability to cope with coher-

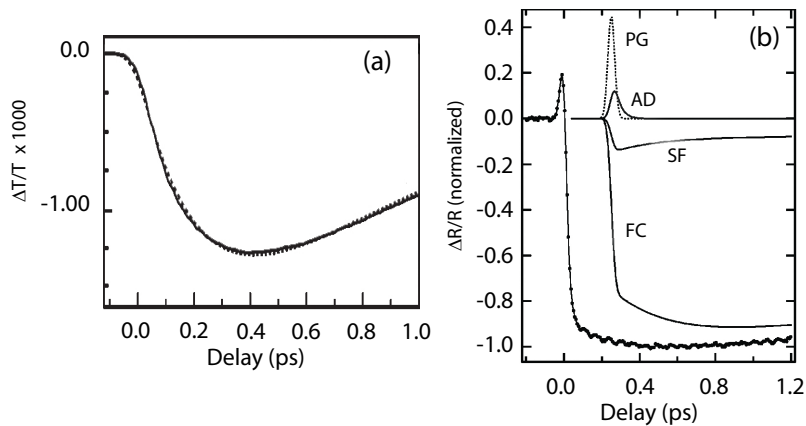


Figure 4.7: Differential transmission/reflectivity dynamics with a 25 fs time-resolution of (a) silver and (b) silicon as reproduced from Sun *et al.*[166] and Sabbah *et al.*[167] respectively. The dynamics in silver is well described with the two-temperature model (dashed line) while the silicon dynamics consist both non-coherent (Free carrier (FC) and state filling (SF)), and coherent (polarization grating (PG), and anisotropic distribution (AD)) processes.

ent effects, the three-temperature model contains a number of free parameters, which means that the model can provide a very good fit to the data even though these parameters might take on unrealistic values. In these cases, a better starting point are the Boltzmann transport equations that include momentum dependence, Coulomb interactions and screening explicitly.[166, 168, 169, 170]

A schematic of the time-scale hierarchy described here can be found in Fig. 4.8, including the heat diffusion and carrier-removal processes that governs the dynamics after the new thermal equilibrium at temperature  $T_1 > T_0$  is reached.

### Observing Photoexcited Dynamics

In the previous section the dynamics following electronic excitation by an ultrashort laser pulse were discussed. Here, the dynamical effects that can be observed in experiments and in particular how the dynamics of strongly correlated materials are of particular interest will be explained.

A pump-probe experiment measures the photoinduced changes in some chosen optical property, for example reflectivity, transmission, absorption, Raman activity or Kerr rotation. As the light-matter interaction primarily takes place via the electrons, a photoinduced process has to affect the electronic (or spin) properties of the material to be observable in pump-probe experiments<sup>2</sup>.

The effects from the initial photoexcitation are schematically shown in Fig.

<sup>2</sup>This is a valid statement in the optical region. Probing instead with x-ray photons, interactions with core-electrons become important and a direct view of dynamical atomic displacements can be obtained.

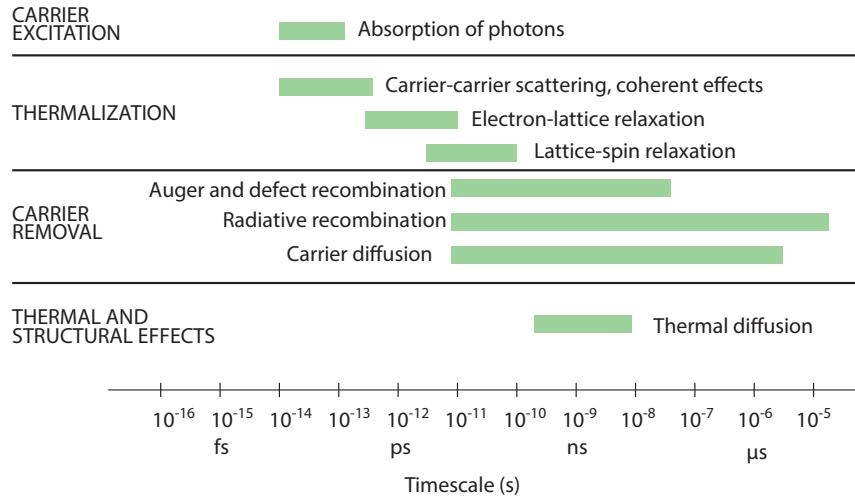


Figure 4.8: The time-scale hierarchy of the different relaxation processes after photoexcitation. The yellow area covers the approximate range of pulse durations in ultrafast experiments. Green bars represent the distribution of time-scales between different materials for a given relaxation process. Modified and reproduced from Fig. 1 in Sundaram and Mazur[164].

4.9 for interband excitation in a semiconductor. In equilibrium, the interband excitation from the valence band to the conduction band is the only allowed transition. After the pump pulse, two additional processes labelled 2 and 3 have the potential to become allowed while the decrease in both the number of initial and final states decreases the probability of process 1 due to Fermi's golden rule. The state-filling process in silicon, see Fig. 4.7(b), is a manifestation of exactly the reduction in probability of process 1. Additionally, the injection of free carriers into the conduction band adds a Drude-like component to the optical conductivity which, through a change in the complex index of refraction, modifies the optical response of the material.[167] This is the free-carrier contribution to the silicon dynamics in Fig. 4.7(b).

In principle, the photoexcitation will also lead to a non-thermal many-body renormalization of the band-gap. For silicon, this effect was found to be negligible[167]. The band-gap in a Mott insulator is on the other hand a direct effect of electron-electron correlations. Photoexcitation either removes or injects, depending on the band structure, electrons in the Hubbard band, effectively doping the material. At a sufficient high fluence, this photodoping is large enough to drive the Mott insulator into a metal by filling control as discussed in Section 2.4. The metallic state obtained after photodoping a Mott insulator is found to be very short-lived, with electron-hole recombination on the sub-ps timescale,[171] as compared to the 100 ps scale in silicon.[167]

In silver and silicon discussed above, the electron-lattice relaxation is only implicitly visible as a decay of the signal from the electronic subsystem. How-

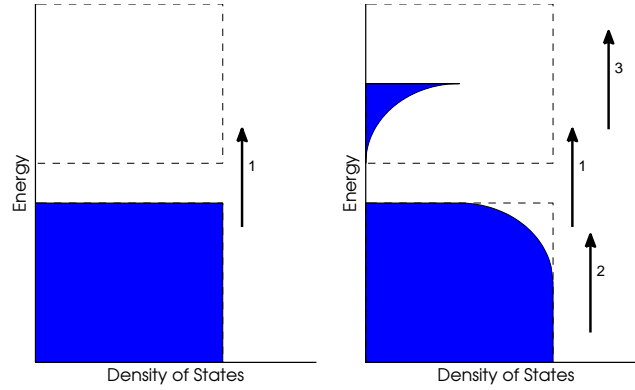


Figure 4.9: Density of states before (left) and after (right) pumping. Before the pump, only process 1 could be initiated by the probe. After being pumped, the two additional processes labeled 2 and 3 is potentially allowed while the probability of process 1 is lowered due to a decrease in both the number of initial and final states. It is clear that the optical properties, which depends on how light can excite electrons, changes drastically after being pumped.

ever, in strongly correlated materials, such as the manganite  $\text{La}_{1-x}\text{Ca}_x\text{MnO}_3$  investigated in **Paper II**, the lattice relaxation can be observed explicitly. This is for example the case in manganites, where the energy transferred into the lattice induces a relaxation of the Jahn-Teller distortion/orbital order. As a consequence, the relative energy of the  $e_g$  orbitals shift and a signal is observed in the experiment.

At longer times, the lattice-spin relaxation tends to randomize the relative spin directions – this process does not occur unless there exists an ordered spin arrangement to start with. The effect of spin-disorder is always visible in homogeneously magnetized samples by the magneto-optical Kerr effect, whereby the rotation of polarization changes according to the magnitude and direction of the magnetization at the sample surface. In the double-exchange metallic state of doped manganites, the spin-disorder drastically decreases the electronic mobility and effectively causes a metal-insulator transition. Thus, also the spin relaxation is visible in manganites as the inter-site  $d-d$  is strongly affected.

Generally, the lattice and spin relaxations can be expected to explicitly contribute to the optical response when the respective degrees of freedom are *correlated*, as opposed to merely *interacting*, with the electrons.

The observed modulations of an optical property  $X$ , as described above, can be connected to the three-temperature model by a first-order expansion

$$\Delta X(t) = \frac{\partial X}{\partial N} \Delta N(t) + \sum_i \frac{\partial X}{\partial T_i} \Delta T(t)_i \quad (4.11)$$

where the index  $i$  goes through the subsystems in question. Hence, the transient

response of  $X$  is proportional, for small  $\Delta N$  and  $\Delta T_i$ , to the non-thermal carrier and subsystem temperature dynamics given by Eq. 4.10.

## 4.2 Raman Spectroscopy

In Raman spectroscopy, inelastically scattered light from a sample is analyzed. Apart from the familiar elastically scattered light, the complex interactions between photons and matter also produce inelastically scattered photons with an energy that is shifted with respect to the incident photons. The shift in energy can be identified with a quasi-particle excitation in the sample, and by collecting photons over a range of energies, a spectrum of low energy excitations in the material is obtained. This effect was first observed 1928 independently by C.V Raman (hence the name of the method)[172] and G. Landsberg and L. Mandelstam,[173] but because the observed quasi-particle spectrum is broadened accordingly to the wavelength content of the incoming photons, the method was not popularized until the advent of affordable laser systems.[174] The excitations observed in Raman spectroscopy on solids can, to a large extent be divided into phonons, magnons or electronic excitations. The momentum,  $k$ , of a photon in the visible or infra-red regions is much smaller than the extension of the Brillouin-zone so that it is possible to approximate the momentum transfer to zero. Photonically induced excitations thus have  $k \approx 0$ ; they belong to the  $\Gamma$ -point of the Brillouin-zone.

A rigorous theoretical treatment of inelastic photon scattering from solids requires an analysis using quantum mechanical many-body theory.[175] From such an analysis, the Raman effect is visualized using an infinite sum of Feynman diagrams, where the simplest diagram involving phonons is a one-loop process consisting of three vertices as shown in Fig. 4.10 and is computed using third order time dependent perturbation theory.[176] The process shown effectively involves an incident photon, a phonon and a scattered photon. If the phonon is created, the energy of the incident photon will, due to energy conservation, be higher than that of the scattered photon: This case is known as Stokes scattering. If, on the other hand, the phonon is already present and instead transfers energy into the process, the energy of the scattered photon will be higher: This is known as anti-Stokes scattering.

With the incident light having frequency  $\omega_i$ , the intensity of scattered light as a function of transferred energy  $\hbar\omega_s = \hbar\omega_i - \hbar\omega$  is proportional to the differential cross-section for the scattering of a photon in the frequency interval  $d\omega$  and angle interval  $d\Omega$ . The cross-section for the Stokes case is

$$\frac{d^2\sigma_{e_i e_s}}{d\Omega d\omega} = V \frac{\omega_s^4}{c^4} [n(\omega) + 1] |e_i^\alpha e_s^\beta \chi'_{\alpha\beta}|^2 \text{Im}T(q, \omega), \quad (4.12)$$

where  $V$  is the scattering volume,  $\chi'$  is the second order electric susceptibility (or, equivalently for small scattering frequencies, susceptibility derivative),  $e_{i(s)}$

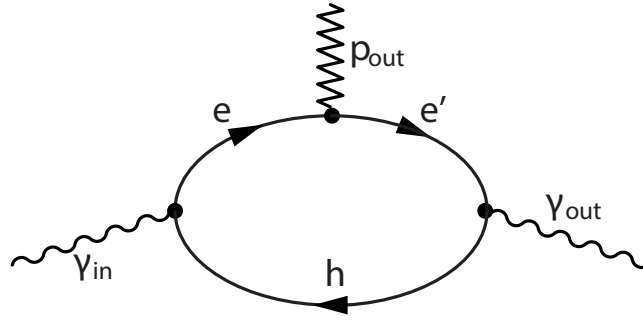


Figure 4.10: Feynman diagram illustrating the lowest order process involved in Raman scattering from phonons. The incident and scattered photons are denoted by  $\gamma_{in}$  and  $\gamma_{out}$  respectively, while  $p$  is the involved phonon. The incident photon interacts with the electronic degree of freedom, creating a (virtual) electron ( $e$ )-hole ( $h$ ) pair. The virtual electron transfers/receives energy to/from a (real) phonon in the Stokes/anti-Stokes case, and is subsequently recombined with the hole, radiating a scattered photon. Compared to the incident photon, the energy of the scattered photon will differ by an amount corresponding to the energy of the involved phonon.

is the polarization vector of the incident (scattered) photon and  $T(q, \omega)$  is the response function, related to fluctuations in the susceptibility,[177] for the excitation in question.  $n(\omega)$  is the Bose-Einstein statistical factor.[13]

Equation 4.12 is composed of three parts, whereof  $V\omega_s^4 [n(\omega) + 1] / c^4$  is a statistical part independent of the material.  $|e_i^\alpha e_s^\beta \chi'_{\alpha\beta}|^2$  is responsible for the selection rules in Raman spectroscopy. By adjusting the polarization of the incident and scattered light, different components of the susceptibility tensor  $\chi'_{\alpha\beta}$  can be reached. This selectivity can be used, together with group theory, to classify excitations and to deduce what the microscopic origin of the observed peaks are. The selection rules, see Sec. 2.2.1, for Raman scattering is derived from  $\Gamma_f \subseteq \Gamma_\chi \otimes A_{1g}$ , where the totally symmetric representation  $A_{1g}$  describes the ground state of the system. The excitations probeable by Raman spectroscopy must therefore have a symmetry that is contained in the symmetric bilinear form  $\chi_{\alpha\beta}$ , i.e  $\Gamma_f \subseteq \Gamma_\chi$ .

Formally,  $\chi_{\alpha\beta}$  is a symmetric bilinear form<sup>3</sup>. As such only excitations transforming according to symmetric representations are (vibrationally) Raman allowed. However, second order scattering, is allowed regardless of the symmetry of the first order excitation, as  $A_{1g} \subseteq \Gamma_x \otimes \Gamma_x$ , for all  $\Gamma_x$ .

The final part of Eq. 4.12,  $\text{Im}T(q, \omega)$ , is a structure factor that gives the spectral shape of the excitations in the probed  $\chi_{\alpha\beta}$  components, for example Lorentzians with or without Fano contributions from electron-phonon interac-

<sup>3</sup>For excitations that behaves symmetrically under time-reversal, such as vibrations and electronic excitations,  $\chi_{\alpha\beta}$  is symmetric. Magnetic excitations are on the other hand anti-symmetric under time-reversal and this is reflected also in the corresponding  $\chi_{\alpha\beta}$ .

tions in the case of homogeneously broadened phonons, Gaussians in the case of inhomogeneously broadened phonons, and the Voigt shape when both processes has to be included.[178, 179]

The frequency  $\omega_0$  of a phonon, at a given temperature, increases with the strength of chemical bonding and decreases with effective mass, while the Lorentzian linewidth  $\Gamma$  is inversely proportional to the phonon lifetime. The intrinsic temperature variations of  $\Gamma$  and  $\omega$  are related to the phonon self-energy via anharmonic decay involving three or more phonons.[180, 181, 182] Experimental deviations from the anharmonic prediction signifies the presence of additional processes such as for example electron-lattice interactions. Such an analysis is used in **Paper VI** in order to study the electron-phonon coupling across the superconducting transition in the 1111 class of iron-pnictide superconductors.

Lifetime broadening can also arise as a result of a disorder-induced increase in the phonon collision rate[183] while the aforementioned Gaussian line-shape arises from a disorder induced distribution in the center frequency  $\omega_0$  reflecting local variations in the immediate surroundings of the oscillator.

## Raman Spectroscopy and Crystal Structure

The number of Raman allowed vibrations is a strongly varying function depending on the space group and Wyckoff position of the constituent atoms. Although a cubic perovskite  $ABO_3$  with space group  $Pm\bar{3}m$  have five atoms in the unit cell, and accordingly  $3N - 3 = 12$  optical vibrations, none of these are Raman active as they all break the inversion symmetry of the crystal.[12] However, any deviation from the highly symmetric  $Pm\bar{3}m$  structure will cause a number of vibrational modes to become Raman active. This is especially true if the distortion is a tilt of the oxygen octahedra as this causes at least a doubling of the unit cell, thus folding modes previously on the border of the Brillouin zone onto the  $\Gamma$ -point.

A second order transition from a high symmetry phase to phase with lower symmetry is often associated with a vibrational soft modes that encodes the shift in atomic position across the phase transition.[13] In the low symmetry phase this soft mode has a frequency that goes toward zero as the high symmetry phase is approached and the mode is frozen in. Perovskites generally exhibit such soft mode behavior in the octahedral tilt mode corresponding to the  $a_{1g}$  tilt-distortion away from  $Pm\bar{3}m$ .[184] The observation of such behavior with isovalent substitution is used in **Paper III** to assign the  $a^- a^- a^-$  antiferrodistortive  $a_{1g}$  tilt mode in  $\text{BiFeO}_3$ .

Figure 4.11, with data from **Papers IV and V**, illustrate, for the dry-hydrated phase transition in  $\text{BaInO}_3\text{H}$ , the way in which Raman spectroscopy can be used to obtain detailed structural information, both by following the evolution of the number of peaks and their disorder-induced broadening.

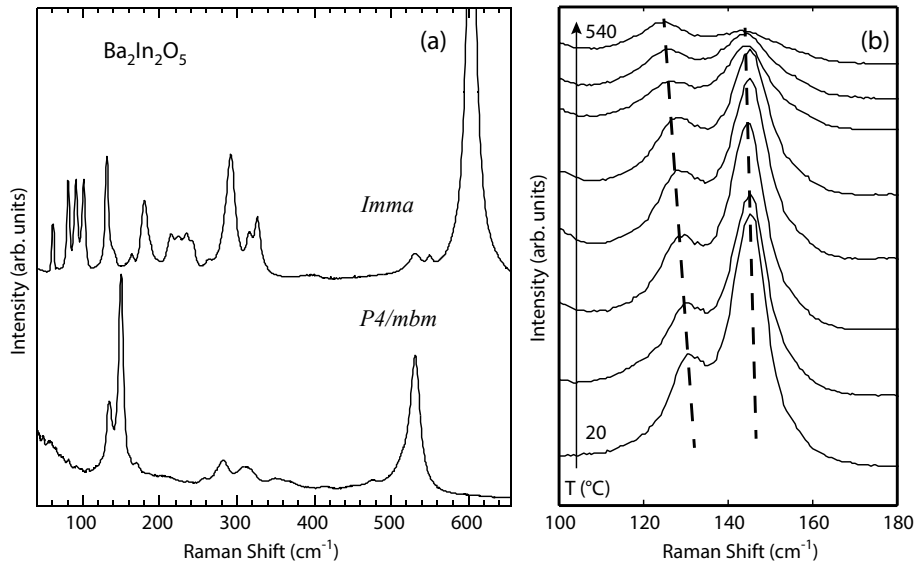


Figure 4.11: The strong Raman–structure relationship is illustrated in (a), exemplified by  $\text{Ba}_2\text{In}_2\text{O}_5$ . A large decrease in the number of Raman active vibrational modes is observed when going from the the low-symmetry  $Imma$  dry phase to the high-symmetry  $P4/mbm$  hydrated phase. In (b) the temperature induced line-width broadening is illustrated. The lower frequency mode is both softened and broadened according to the Klemens model[180]  $\Gamma(T) \sim [1 + 2n(T)]$ , while the higher frequency mode exhibits an anomalously large broadening as a consequence of disorder effects.

### Instrumentation

The Raman measurements presented in this thesis are performed with a DILOR XY-800 triple grating spectrometer connected to a  $\text{Ar}^+/\text{Kr}^+$  laser with laser lines ranging from 458–676 nm. As all of the investigated samples consists of small micro crystallites, measurements from well defined surfaces require the use of a microscope objective to focus the laser light. The working principle of the spectrometer in double subtractive configuration is shown in Fig. 4.12. The light from the laser passes through the microscope objective, interacts with the sample and the backscattered light enters the spectrometer for analysis. In double subtractive configuration, the first two gratings act as a band-pass filter that rejects the very strong elastically scattered light ( $I_{\text{Raman}}/I_{\text{Elastic}} < 10^{-5}$ ). By rotating the two gratings in tandem the acceptance wavelengths of the band-pass filter can be tuned to the spectral region of interest. The inelastically scattered light is then dispersed by the third grating and imaged on a CCD-camera, where each row of pixels collects photons in a narrow wavenumber range given by the rotation angle of the dispersive third grating.

With the strongest laser line at 514.5 nm each measurement gives a spectral

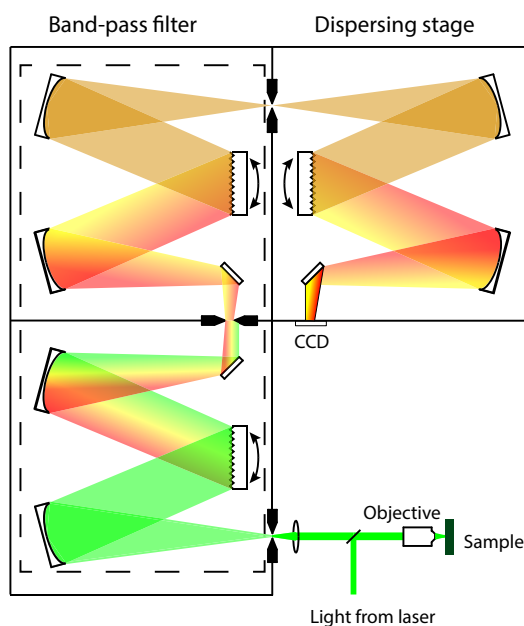


Figure 4.12: Schematic view of the working principle behind the double subtractive configuration. The first two gratings, inside the dashed rectangle, act as a band-pass filter that rejects the strong elastically scattered light. This is illustrated in the figure as the loss of green light, representing the laser at 514 nm, at the slit connecting the first and second Czerny-Turner stage. The final spectral resolution is determined by the opening widths of the slits between each of the three stages, although increased resolution leads to a reduced number of collected photons at the CCD.

window  $\sim 630 \text{ cm}^{-1}$  in width, with measurements routinely done as close as  $\sim 30 \text{ cm}^{-1}$  from the laser line. For some applications, for example second-order scattering and O-H stretch spectroscopy, a spectral window of  $630 \text{ cm}^{-1}$  is too small for the whole spectrum to be collected in one measurement. For these cases, it is possible to switch to a single grating configuration with lower spectral resolution but with a considerably broader spectral window of  $\sim 1600 \text{ cm}^{-1}$ . In addition, this setup is favorable for samples with low scattering cross section as the number of optical components, and thus loss of intensities, are significantly decreased.



# 5

## Summary of Appended Papers

In this chapter, the most important results in each of the appended papers are discussed. A brief introduction is followed by an explanation of the results and conclusions suited to a broader scientific public. My contribution to each paper is also stated.

### 5.1 Paper I

#### **Femtosecond optical-reflectivity measurements of lattice-mediated spin repulsions in photoexcited LaCoO<sub>3</sub> thin-films**

Johan Bielecki, Diana Rata and Lars Börjesson

Electron-lattice interactions have been found, indirectly, to be an important factor in the spin-state transition in LaCoO<sub>3</sub>. [83, 85] However, in which way and to which degree is not understood, although it is hypothesized that the population of the larger high-spin Co ion is suppressed due to the cooperative "high-spin repulsions" first conjectured by Goodenough in the 1950's. [2]

In this paper, a time-resolved study on LaCoO<sub>3</sub> is presented, with the aim to study the temperature evolution of the electron and lattice dynamics across the spin state transition. Two main results are obtained. First it is shown that time-resolved spectroscopy offers an accurate measurement of the low-spin fraction. Second, the temporal resolution makes it possible to disentangle the lattice mediated high-spin repulsion from the thermally activated population.

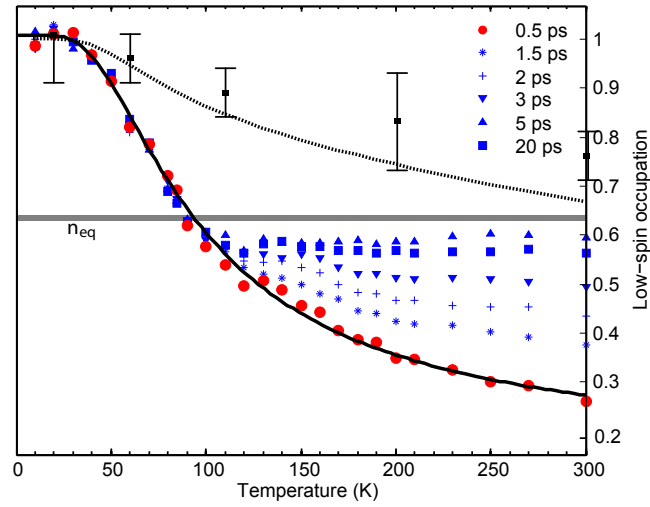


Figure 5.1: The low-spin fraction,  $n_{LS}$ , as a function of temperature. The broken line and squares with error-bars are estimations from bulk  $\text{LaCoO}_3$ . [83, 85] The symbols shows the measured  $n_{LS}$  in thin-film  $\text{LaCoO}_3$  as a function of delay after photoexcitation, with the solid line being a fit to the Fermi distribution. Finally, the grey shaded line is the equilibrium  $n_{LS}$  in the thin-film sample. [97]

In more detail, photoexcitation releases a low-spin population exactly in accordance with Fermi statistics. At the timescale of electron-lattice relaxation a pronounced increase of the low-spin population occurs, giving the first explicit observation of the lattice mediated high-spin repulsion effect, see Fig. 5.1. Finally, the low-spin population measured in equilibrium [97] is found to be determined exclusively by the high-spin repulsion.

*My contribution was in designing the study, performing the time resolved measurements, interpreting the results, writing the manuscript and setting up the lab.*

## 5.2 Paper II

### Two Component Heat Diffusion Observed in $\text{LaMnO}_3$ and $\text{La}_{0.7}\text{Ca}_{0.3}\text{MnO}_3$

Johan Bielecki, Ralf Rauer, Ezio Zanghellini, Robert Gunnarsson, Katrin Dörr and Lars Börjesson

Manganites are one of the most studied class of strongly correlated perovskites, with many interesting properties such as charge/orbital order, strong electron-lattice couplings, double exchange, metal-insulator transitions and colossal

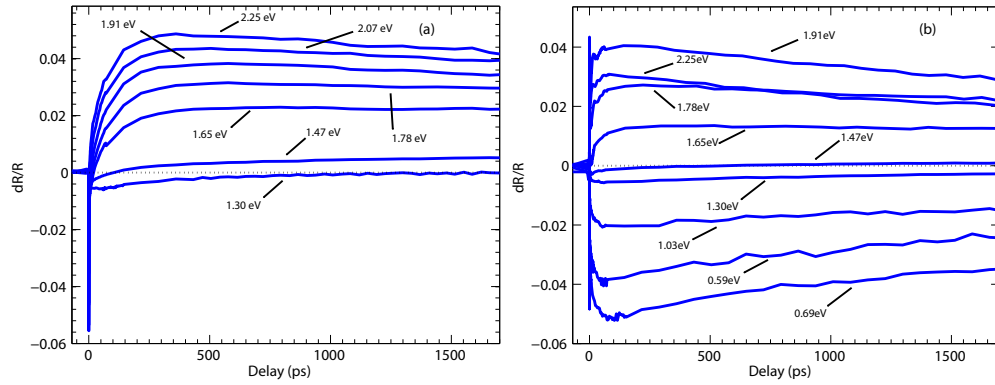


Figure 5.2: Transient reflectivity in (a) LMO and (b) LCMO for different probe energies when pumping with 1.6 eV. Note in particular the change in the final relaxation time when changing probe energy and the zero crossing ( $\sim 100$  ps, LMO and  $\sim 550$  ps LCMO) when probing with 1.47 eV, features whose explanation require the two-component heat diffusion.

magnetoresistance.[20] In this paper the low-temperature electron, lattice, and spin dynamics of the anti-ferromagnetic insulator  $\text{LaMnO}_3$  and the ferromagnetic double-exchange metal  $\text{La}_{0.7}\text{Ca}_{0.3}\text{MnO}_3$  are investigated by resonant pump-probe reflectance spectroscopy.

Probing the high-spin, inter-site, d-d transition as a function of time delay and probe energy, we compare the responses of the Mott insulator and the double-exchange metal to the photoexcitation, see Fig. 5.2. Attempts have previously been made to describe the subpicosecond dynamics of colossal magnetoresistance manganites in terms of a phenomenological three-temperature model describing the energy transfer between the electron, lattice, and spin subsystems followed by a comparatively slow exponential decay back to the ground state. Here it is shown that an additional component in the long-term relaxation due to film-to-substrate heat diffusion is present.

*My contribution was in designing the study, performing the time resolved measurements, interpreting the results, writing the manuscript and taking part in setting up the lab.*

## 5.3 Paper III

### Structural and Magnetic Properties of Isovalently Substituted Multiferroic $\text{BiFeO}_3$ : Insights from Raman spectroscopy

Johan Bielecki, Peter Svedlindh, Dessie T. Tibebe, Shengzhen Cai, Sten-G. Eriksson, Lars Börjesson, and Christopher S. Knee

Multiferroic  $\text{BiFeO}_3$  exhibit many prerequisites for being practically useful in

new types of magneto-electric devices.[9] However, the presence of a cycloidal modulation of the Fe spins causes the magneto-electric effects to cancel out on average. Different routes has been proposed for suppressing the cycloidal spin order, for example epitaxial strain[60] and atomic substitution[61].

Isovalent substitution on the Bi site leads to structural phase transitions with a complicated phase diagrams that so far has proven ambiguous from diffraction data. In this paper, Raman spectroscopic investigations into the structure of three different substitution series are presented, complemented with X-ray diffraction and magnetization measurements. Vibrational spectroscopy offers a good complement to the previously published diffraction results as atomically local distortions can be probed at the same time as impurity phases are more easily avoided as the probed volume is much smaller.

The structural transitions observed with Raman spectroscopy are consistent with the latest diffraction results,[64] and, together with the magnetization curves, our data shows that the spin-cycloid is only completely destroyed when a structural transition away from the multiferroic  $R3c$  phase takes place. However, a partial suppression was observed within the  $R3c$  phase that coincides with the nonuniform ferroelectric polarization induced by A-site substitution as observed with Raman spectroscopy.

In addition, the phonon assignment in  $\text{BiFeO}_3$  is controversial, with many different assignments reported in the literature.[68, 69] By comparing the vibrational frequencies within the  $R3c$  phase, we identify a pseudo-soft mode behaviour of the  $220 \text{ cm}^{-1}$  mode, as can be seen in Fig. 5.3, indicating a  $A_1$  mode with a  $a^-a^-a^-$  antiferrodistortive character.[184] This supports a previous assignment done by comparing DFT calculations[70, 71] with the experimental angular dispersion curves.[69]

*My contribution was in performing the Raman measurements, interpreting the results, writing a substantial part of the manuscript, and taking a large part in designing the study.*

## 5.4 Paper IV

### Local Structure and Phonon Assignment in Brownmillerite Type Oxide $\text{Ba}_2\text{In}_2\text{O}_5$

Johan Bielecki, Stewart F. Parker, Dharshani Ekanayake, Lars Börjesson, and Maths Karlsson

Proton conducting oxides have a potential in energy applications as intermediate-temperature solid oxide fuel cells.[99, 100] The acceptor doping, such as  $\text{In}^{3+}$  substituted for  $\text{Zr}^{4+}$  in  $\text{BaZrO}_3$ , creates an oxygen-deficient structure, in which protons can be incorporated by hydration. The brownmillerite compound  $\text{Ba}_2\text{In}_2\text{O}_5$  has been suggested as parent compound for a new class of intermediate temperature proton-conductors with ordered oxygen vacancies. Pro-

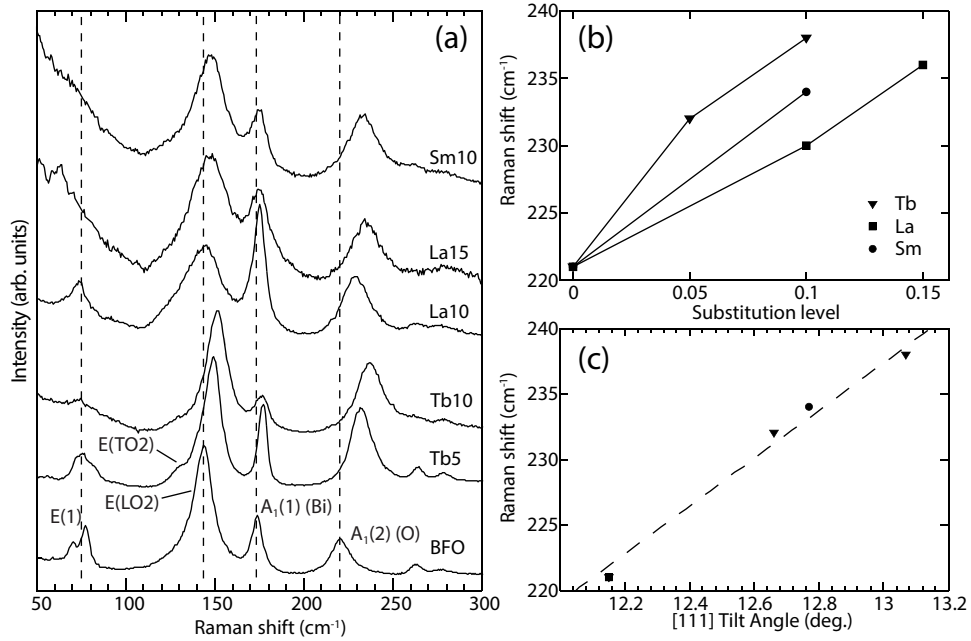


Figure 5.3: (a) Raman spectra in the  $R3c$  phase. The intensity of the  $E(1)$  mode and the two Fe derived modes at  $\sim 270$   $\text{cm}^{-1}$  seems to decrease with nonuniform ferroelectric polarization and the partial destruction of the spin cycloid. The  $A_1(2)(O)$  mode is the pseudo-soft oxygen-tilt mode discussed in the text. (b) The frequency of the  $A_1(2)(O)$  as a function of substitution. (c) The frequency of the  $A_1(2)(O)$  as a function of octahedral tilt angle, showing the linear dependence characteristic for the pseudo-soft  $a^-a^-a^-$  antiferrodistortive mode.

ton conductivity occurs through a sequence of reorientational hydrogen motion followed by hydrogen transfer between nearby oxygens. The transfer process is expected to be related to vibrational modes involving the oxygens towards which the protons are bound.[105, 106] Consequently, vibrational spectroscopy could potentially be a powerful tool for investigating the role of phonons in this process. However, few spectroscopic studies on  $\text{Ba}_2\text{In}_2\text{O}_5$ , and brownmillerites in general, has been published and no assignment of the vibrational spectrum to specific atomic motions exists.

In this paper we present the first detailed investigation regarding the vibrational properties of  $\text{Ba}_2\text{In}_2\text{O}_5$ . Using a combination of IR, Raman and DFT calculations, a large majority of the observed phonons are assigned in the dry phase, and a schematic phonon assignment is shown in Fig. 5.4. A comparison between the calculations and experimental results reveal several distinct Raman spectroscopic fingerprints that can be used to distinguish between the very similar  $Imma$ ,  $Pnma$ , and  $Ibm2$  varieties of the brownmillerite structure.

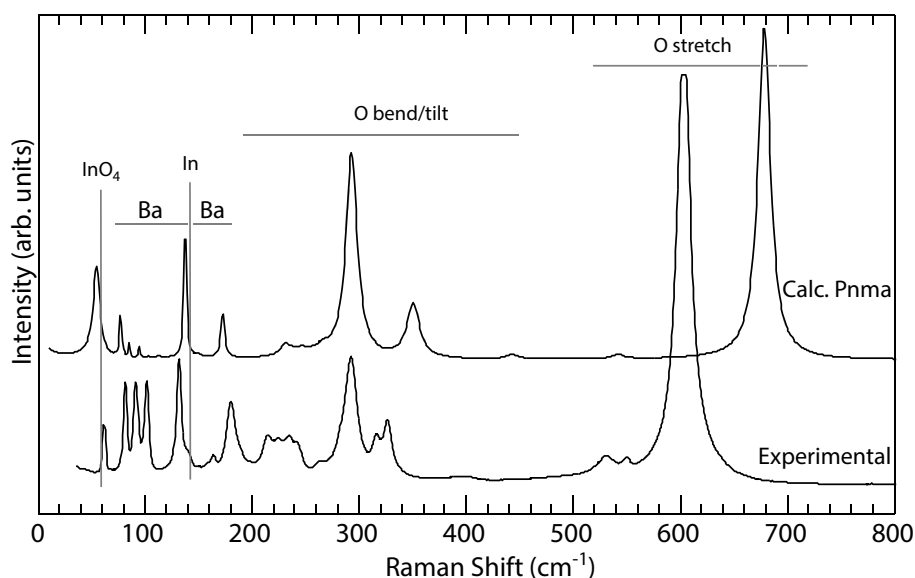


Figure 5.4: Experimental and calculated Raman spectra in the dry of  $\text{Ba}_2\text{In}_2\text{O}_5$ . The phonon assignments are indicated in the figure by the kind of vibrational motion in different spectral regions.

On the other hand, a less satisfactory agreement between experimental data and calculations is obtained the hydrated phase, indicating that the hydrated structure is more complicated than what has been proposed earlier.

*My contribution was in designing the study, performing the Raman measurements, interpreting the results, and writing the manuscript.*

## 5.5 Paper V

### Local structure and hydration/dehydration properties of proton conducting brownmillerite $\text{Ba}_2\text{In}_2\text{O}_5$ investigated with Raman spectroscopy

Johan Bielecki, Stewart F. Parker, Seikh Mohammad Habibur Rahman, Christopher S. Knee, Sten-G. Eriksson, Lars Börjesson, and Maths Karlsson

As a continuation of the phonon assignment presented in Paper IV, this paper aims to further understand the local structure in  $\text{Ba}_2\text{In}_2\text{O}_5$  by investigating the structural dynamics during the hydrated-dry transition. Starting with  $\text{BaInO}_3\text{H}$ , the transition towards  $\text{Ba}_3\text{In}_3\text{O}_5$  occurs gradually *via* the release of water vapor with increasing temperature. Between the hydrated and dry phases the Raman spectra shows clear signs of an intermediate phase. As can

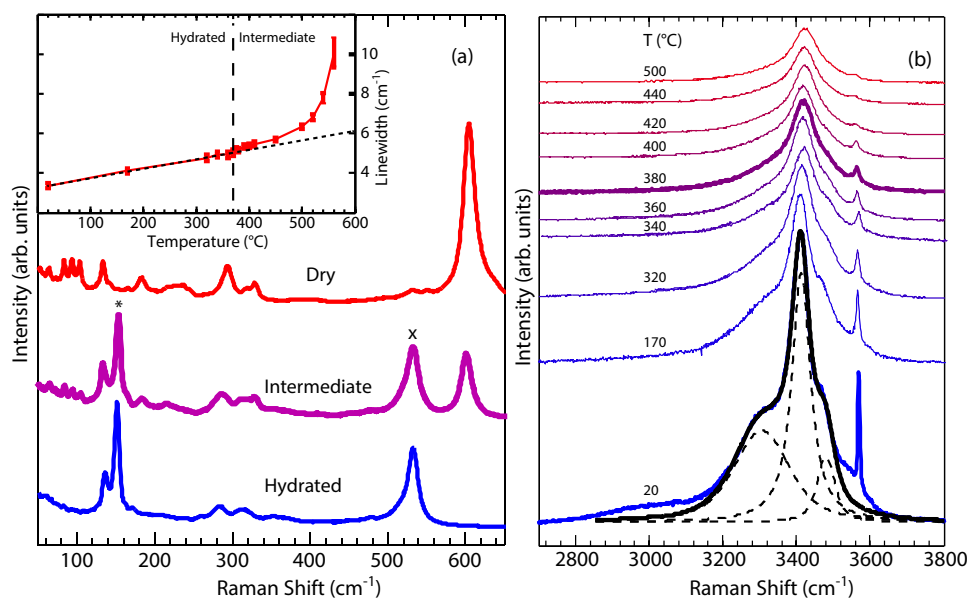


Figure 5.5: (a) Raman spectra of the dry, intermediate and hydrated  $\text{Ba}_2\text{In}_2\text{O}_5$  phases. The vibrational modes marked with \* and x are the In(1) and In-O modes induced by protons and additional oxygens that distinguish the intermediate phase Raman spectra from that in the dry phase. The inset shows the anomalous broadening of the \* mode discussed in the text. (b) The O-H stretch band as a function of temperature. The lack of a distinct band below  $3000\text{ cm}^{-1}$  is not consistent with the previously proposed proton structure.[101]

be deduced from the Raman spectra in Fig. 5.5, this intermediate phase is closer to the dry crystal structure than the hydrated.

The Raman spectra reveals that the intermediate phase differ from the dry by a displaced In position caused by the electrostatic hydrogen pull on the in-plane oxygen. The In displacement becomes locally disordered as the proton content decrease, resulting in the anomalous line-width broadening shown in the inset of Fig. 5.5(a).

Further, an analysis of the O-H stretch area, using both Raman and inelastic neutron spectroscopy, shows that the hydrated-intermediate transition occurs at a hydration level of  $\sim 35\%$ . Consistent with our findings from **Paper IV**, the lack of a strong the O-H stretch band below  $3000\text{ cm}^{-1}$ , see Fig. 5.5(b), is not consistent with the local structure predicted from DFT calculations.[101]

*My contribution was in designing the study, performing the Raman measurements, interpreting the results, and writing the manuscript.*

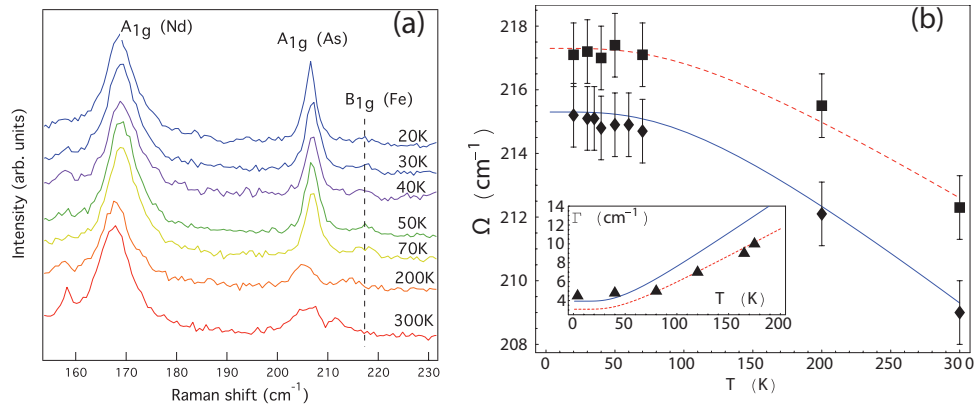


Figure 5.6: (a) Measured Raman spectra as a function of temperature on  $\text{NdFeAsO}_{1-x}\text{F}_x$  ( $x = 0.12$ ). (b) The theoretical fits (lines) to the Raman shift for  $\text{NdFeAsO}_{0.88}\text{F}_{0.12}$  (boxes) and  $\text{CeFeAsO}_{0.84}\text{F}_{0.16}$  (diamonds). The inset shows the lifetime measured on  $\text{CaFe}_2\text{As}_2$  taken from [145]

## 5.6 Paper VI

### Anharmonic softening of Raman active phonons in iron-pnictides: Estimating the Fe isotope effect due to anharmonic expansion

M. Granath, Johan Bielecki, Joakim Holmlund and Lars Börjesson

The most important of the many unanswered questions regarding high temperature superconductors is about the nature of the effectively attractive force between electrons in a cooper pair. In the widely accepted BCS theory, overscreening from phonons is shown to be the glue in ordinary superconductors, but it is widely believed that the glue in the cuprates and iron-pnictides cannot be phonons, and instead several other mechanisms including magnetic fluctuations and electronic correlations has been put forth.

In this paper we investigate, by combining Raman spectroscopy and perturbative phonon-phonon calculations, the role of phonons in the newly discovered iron-pnictide class of superconductors. Several previous calculations and experiments indicates that the electron-phonon coupling is too weak to account for the high transition temperatures ( $\sim 50\text{K}$ ). Using Raman spectroscopy, we determine the temperature dependence of the optical phonons in close to optimally doped  $\text{CeFeAsO}_{1-x}\text{F}_x$  ( $x = 0.16$ ) and  $\text{NdFeAsO}_{1-x}\text{F}_x$  ( $x = 0.12$ ). We observe a softening of the phonons as the temperature increases and there is no noticeable anomaly associated with crossing  $T_c$ , see Fig. (5.6).

The calculations, based on anharmonic phonon-phonon coupling gives an approximation of both the lifetime (width) and peak shift of the  $B_{1g}\text{Fe}$  phonon, with the electron-phonon interaction excluded. Only one fitting parameter is needed to relate this expression to experimentally measured spectra. We find

that the  $B_{1g}$ Fe phonon follows the theoretical prediction and that the electron-phonon coupling is sufficiently weak to be invisible in our Raman spectra.

With this in mind, we continue with an analysis of the effect on  $T_c$  by isotopic substitution on the Fe site. This effect has been reported as surprisingly large given the experimental indications of a weak electron-phonon interaction. In the anharmonic approximation, an isotopic substitution causes a lattice expansion that can be expressed in terms of an effective pressure. Using previously published pressure dependence on  $T_c$ , an isotope exponent of  $\alpha \approx 0.06$  is found. The isotope effect found experimentally is almost an order of magnitude higher,  $\alpha = 0.4$ .

The two conflicting observations imply a serious challenge for any theory of superconductivity in the iron-pnictides.

*My contribution was in performing parts of the Raman measurements and taking part in the interpretation and discussion of the results.*

## Acknowledgments

I am grateful to the many persons who have contributed to the scientific work presented here, this thesis would not have been possible without you. My supervisor Lars Börjesson for always encouraging my work. Ralf Rauer for putting me on track the first months of my PhD studies. Chris Knee for stimulating discussions and samples. Ezio Zanghellini for invaluable help with technicalities in the lab and the many discussions on physics. Joakim Holmlund for introducing me to Raman scattering. Maths Karlsson for supervising my work on brownmillerites. I would also like to thank Mats Granath for the iron-pnictide collaboration, Peter Svedlindh for magnetization measurements, Habib for a whole bunch of brownmillerite samples, and Diana Rata for the  $\text{LaCoO}_3$  thin-films. Aleks, Pelle and Johan M for the interesting hydrogen-bond projects.

I would also like to thank all the members of the Condensed Matter Physics group for making the five years as a PhD student here so enjoyable.

But most of all I would like to thank my wonderful family and especially Julia, your support has meant everything.

# Bibliography

- [1] R. Kusters, J. Singleton, D. Keen, R. McGreevy, and W. Hayes, *Physica B* **155**, 362 (1989).
- [2] J. B. Goodenough, *J. Phys. Chem. Solids* **6**, 287 (1958).
- [3] G. A. Smolenskii, V. A. Isupov, and A. I. Agranovskaya, *Sov. Phys. Solid State* **1**, 150 (1959).
- [4] S. Roberts, *Phys. Rev.* **71**, 890 (1947).
- [5] H. Iwahara, T. Esaka, H. Uchida, and N. Maeda, *Solid State Ionics* **3-4**, 359 (1981).
- [6] J. F. Schooley, W. R. Hosler, and M. L. Cohen, *Phys. Rev. Lett.* **12**, 474 (1964).
- [7] C. H. Kim, G. Qi, K. Dahlberg, and W. Li, *Science* **327**, 1624 (2010).
- [8] M. Imada, A. Fujimori, and Y. Tokura, *Rev. Mod. Phys.* **70**, 1039 (1998).
- [9] G. Catalan and J. F. Scott, *Adv. Mater.* **21**, 2463 (2009).
- [10] C. J. Howard and H. T. Stokes, *Acta Cryst.* **B54**, 782 (1998).
- [11] A. M. Glazer, *Acta Cryst.* **B28**, 3384 (1972).
- [12] M. S. Dresselhaus, G. Dresselhaus, and A. Jorio, *Group Theory, Applications to the Physics of Condensed Matter* (Springer-Verlag, Berlin, 2008).
- [13] W. Hayes and R. Loudon, *Scattering of light by crystals* (John Wiley and Sons, New York, 1978).
- [14] C. J. Ballhausen, *Introduction to Ligand Field Theory* (McGraw-Hill Book Company, New York, 1962).
- [15] F. J. Kahn, P. S. Pershan, and J. P. Remeika, *Phys. Rev.* **186**, 891 (1969).
- [16] A. Zenkov, *Opt. Spectrosc.* **98**, 856 (2005).

- 
- [17] J. Zaanen and G. A. Sawatzky, *J. Solid State Chem.* **8**, 88 (1990).
- [18] J. Zaanen, G. A. Sawatzky, and J. W. Allen, *Phys. Rev. Lett.* **418**, 55 (1985).
- [19] R. Rauer, M. Rübhausen, and K. Dörr, *Phys. Rev. B* **73**, 092402 (2006).
- [20] E. Dagotto, T. Hotta, and A. Moreo, *Phys. Rep.* **344**, 1 (2001).
- [21] P. W. Anderson, *Phys. Rev.* **115**, 2 (1959).
- [22] J. B. Torrance, P. Lacorre, A. I. Nazzal, E. J. Ansaldo, and C. Niedermayer, *Phys. Rev. B* **45**, 8209(R) (1992).
- [23] J. Goodenough, *Phys. Rev.* **100**, 564 (1955).
- [24] J. Kanamori, *J. Phys. Chem. Solids* **10**, 87 (1958).
- [25] H. Jahn and E. Teller, *Proc. Roy. Soc.* **A161**, 220 (1937).
- [26] J.-S. Zhou, J.-Q. Yan, and J. B. Goodenough, *Phys. Rev. B* **71**, 220103 (2005).
- [27] R. von Helmolt, J. Wecker, B. Holzapfel, L. Schultz, and K. Samwer, *Phys. Rev. Lett.* **71**, 2331 (1993).
- [28] T. Tokura, A. Urushibara, Y. Moritomo, A. Asamitsu, Y. Tomioka, T. Arima, and G. Kido, *Mat. Sci. Eng. B* **31**, 187 (1995).
- [29] E. Dagotto and Y. Tokura, *MRS Bulletin* **33**, 1037 (2008).
- [30] E. Dagotto, *Science* **309**, 257 (2005).
- [31] G. Jonker and J. van Santen, *Physica* **16**, 337 (1950).
- [32] C. Zener, *Phys. Rev.* **81**, 440 (1951).
- [33] C. Zener, *Phys. Rev.* **82**, 403 (1951).
- [34] P. Anderson and H. Hasegawa, *Phys. Rev.* **100**, 675 (1955).
- [35] P. DeGennes, *Phys. Rev.* **118**, 141 (1960).
- [36] A. Millis, P. Littlewood, and B. Shraiman, *Phys. Rev. Lett.* **74**, 5144 (1995).
- [37] H. Hwang, S.-W. Cheong, P. Radaelli, M. Marezio, and B. Batlogg, *Phys. Rev. Lett.* **75**, 914 (1995).
- [38] E. Wollan and W. Koehler, *Phys. Rev.* **100**, 545 (1955).

- [39] P. Schiffer, A. Ramirez, W. Bao, and S.-W. Cheong, *Phys. Rev. Lett.* **75**, 3336 (1995).
- [40] J. van den Brink, G. Khaliullin, and D. Khomskii, arXiv:cond-mat/0206053.
- [41] Y. Tokura and N. Nagaosa, *Science* **288**, 462 (2000).
- [42] K. Tobe, T. Kimura, Y. Okimoto, and Y. Tokura, *Phys. Rev. B.* **64**, 184421 (2001).
- [43] N. Kovaleva, A. Boris, C. Bernhard, A. Kulakov, A. Pimenov, A. Balbashov, G. Khaliullin, and B. Keimer, *Phys. Rev. Lett.* **93**, 147204 (2004).
- [44] S. Grenier, J. Hill, W. Ku, Y.-J. Kim, K. Thomas, S.-W. Cheong, Y. Tokura, and Y. Tomioka, *Phys. Rev. Lett.* **94**, 047203 (2005).
- [45] J. Kanamori, *J. App. Phys.* **31**, 14S (1960).
- [46] D. Akahoshi, M. Uchida, Y. Tomioka, T. Arima, Y. Matsui, and Y. Tokura, *Phys. Rev. Lett.* **90**, 177203 (2003).
- [47] M. Uehara, S. Mori, C. Chen, and S.-W. Cheong, *Nature* **399**, 560 (1999).
- [48] S. Mori, C. Chen, and S.-W. Cheong, *Nature* **392**, 473 (1998).
- [49] M. Rini, R. Tobey, N. Dean, J. Itatani, Y. Tomioka, Y. Tokura, R. Schoenlein, and A. Cavalleri, *Nature* **449**, 72 (2007).
- [50] N. A. Hill, *J. Phys. Chem. B* **104**, 6694 (2000).
- [51] D. Lebeugle, D. Colson, A. Forget, M. Viret, A. M. Bataille, and A. Gukasov, *Phys. Rev. Lett.* **100**, 227602 (2008).
- [52] S. V. Kiselev, G. S. Zhdanov, and R. P. Ozerov, *Sov. Phys.-Dokl.* **145**, 1255 (1962).
- [53] J. Wang, J. B. Nheaton, H. Zheng, V. Nagarajan, S. B. Ogale, B. Liu, D. Viehland, V. Vaithyanathan, D. G. Schlom, U. V. Waghmare, N. A. Spaldin, K. M. Rabe, *et al.*, *Science* **299**, 1719 (2003).
- [54] T. Higuchi, Y.-S. Liu, P. Yao, P.-A. Glans, J. Guu, C. Chang, Z. Wu, W. Sakamoto, N. Itoh, T. Shimura, T. Yogo, and T. Hattori, *Phys. Rev. B* **78**, 085106 (2008).
- [55] I. Sosnowska, T. Peterlin-Neumaier, and E. Steichele, *J. Phys. C: Solid State Phys.* **15**, 4835 (1982).
- [56] G. Thornton, B. C. Tofield, and A. W. Hewat, *J. Solid State Chem.* **61**, 301 (1986).

- [57] A. Palewicz, I. Sosnowoska, R. Przenioslo, and A. W. Hewat, *Acta Phy. Pol. A* **117**, 296 (2010).
- [58] M. Fiebig, *J. Phys. D: Appl. Phys.* **38**, R123 (2005).
- [59] S.-T. Zhang, Y. Zhang, M.-H. Lu, C.-L. Du, Y.-F. Cheng, Z.-G. Liu, Y.-Y. Zhu, N.-B. Ming, and X. Q. Pan, *Appl. Phys. Lett.* **88**, 162901 (2006).
- [60] T. Zhao, A. Scholl, F. Zavliche, K. Lee, M. Barry, A. Doran, M. P. Cruz, Y. H. Chu, C. Ederer, N. A. Spaldin, R. R. Das, D. M. Kim, *et al.*, *Nature Mater.* **5**, 823 (2006).
- [61] I. Sosnowska, W. Schafer, W. Kockelmann, K. H. Andersen, and I. O. Troyanchuk, *Appl. Phys. A* **74**, 1040 (2002).
- [62] I. O. Troyanchuk, M. V. Bushinksy, D. V. Karpinsky, O. S. Mantytskaya, V. V. Fedotova, and O. I. Prochnenko, *Phys. Solidi B* **246**, 1901 (2009).
- [63] R. D. Shannon, *Acta Cryst.* **A32**, 751 (1976).
- [64] D. A. Rusakov, A. M. Abakumov, K. Yamaura, A. A. Belik, G. Van Tendeloo, and T.-M. Eiji, *Chem. Mater.* **23**, 285 (2011).
- [65] S. Karimi, I. M. Reaney, Y. Han, J. Pokorny, and I. Sterianou, *J. Mater. Sci.* **44**, 5102 (2009).
- [66] I. O. Troyanchuk, D. V. Karpinsky, M. V. Bushinksy, V. A. Khomchenko, G. N. Kakazei, J. P. Araujo, M. Tovar, S. V., V. Efimov, and A. L. Kholkin, *Phys. Rev. B* **83**, 054109 (2011).
- [67] S. Saxin and C. S. Knee, *J. Solid State Chem.* **184**, 1576 (2011).
- [68] C. Beekman, A. A. Reijnders, Y. S. Oh, S. W. Cheong, and K. S. Burch, *Phys. Rev. B* **86**, 020403(R) (2012).
- [69] J. Hlinka, J. Pokorny, S. Karimi, and I. M. Reaney, *Phys. Rev. B* **83**, 020101(R) (2011).
- [70] M. Goffinet, P. Hermet, D. I. Bilc, and P. Ghosez, *Phys. Rev. B* **79**, 014403 (2009).
- [71] P. Hermet, M. Goffinet, J. Kreisel, and P. Ghosez, *Phys. Rev. B* **75**, 220102(R) (2007).
- [72] K. Huang, H. Y. Lee, and J. B. Goodenough, *J. Electrochem. Soc.* **145**, 3220 (1998).
- [73] M. A. Senariz-Rodriguez and J. B. Goodenough, *J. Solid State Chem.* **116**, 224 (1995).

- [74] J. Zhou, J. Yan, and J. Goodenough, Phys. Rev. B **71**, 220103 (2005).
- [75] S. W. Biernacki, Phys. Rev. B **74**, 184420 (2006).
- [76] A. Ishikawa, J. Nohara, and S. Sugai, Phys. Rev. Lett. **93**, 136401 (2004).
- [77] M. Korotin, S. Ezhov, I. Solovyev, V. Anisimov, D. Khomskii, and G. Sawatzky, Phys. Rev. B **54**, 5309 (1996).
- [78] D. Phelan, D. Louca, S. Rosenkranz, S.-H. Lee, Y. Qiu, P. J. Chupas, R. Osborn, H. Zheng, J. F. Mitchell, J. R. D. Copley, J. L. Sarrao, and Y. Moritomo, Phys. Rev. Lett. **96**, 027201 (2006).
- [79] M. J. R. Hoch, S. Nellutla, J. van Tol, E. S. Choi, J. Lu, H. Zheng, and J. F. Mitchell, Phys. Rev. B. **79**, 214421 (2009).
- [80] Y. Kobayashi, T. S. Naing, M. Suzuki, M. Akimitsu, K. Asai, K. Yamada, J. Akimitsu, P. Manuel, T. J. M., and S. G., Phys. Rev. B **72**, 174405 (2005).
- [81] C. Zobel, M. Kriener, D. Bruns, J. Baier, M. Gruninger, T. Lorenz, P. Reutler, and A. Revcolevschi, Phys. Rev. B **66**, 020402 (2002).
- [82] A. Podlesnyak, S. Streule, J. Mesot, M. Medarde, E. Pomjakushina, K. Conder, A. Tanaka, M. W. Haverkort, and D. I. Khomskii, Phys. Rev. Lett. **97**, 247208 (2006).
- [83] M. W. Haverkort, Z. Hu, J. C. Cezar, T. Burnus, H. Hartmann, M. Reuther, C. Zobel, T. Lorenz, A. Tanaka, N. B. Brookes, H. H. Hsieh, H. J. Lin, *et al.*, Phys. Rev. Lett. **97**, 176405 (2006).
- [84] S. Yamaguchi, Y. Okimoto, H. Taniguchi, and Y. Tokura, Phys. Rev. B **53**, R2926 (1996), ISSN 0163-1829.
- [85] T. Kyômen, Y. Asaka, and M. Itoh, Phys. Rev. B **71**, 024418 (2005).
- [86] T. Kyômen, Y. Asaka, and M. Itoh, Phys. Rev. B **67**, 144424 (2003).
- [87] R. F. Klie, J. C. Zheng, Y. Zhu, M. Varela, J. Wu, and C. Leighton, Phys. Rev. Lett. **99**, 047203 (2007).
- [88] V. Křápek, P. Novák, J. Kuneš, D. Novoselov, D. M. Korotin, and V. I. Anisimov, Phys. Rev. B **86**, 195104 (2012).
- [89] D. Fuchs, C. Pinta, T. Schwarz, P. Schweiss, P. Nagel, S. Schuppler, R. Schneider, M. Merz, G. Roth, and H. von Loehneysen, Phys. Rev. B **75**, 144402 (2007).
- [90] D. Fuchs, E. Arac, C. Pinta, S. Schuppler, R. Schneider, and H. von Loehneysen, Phys. Rev. B **77**, 014434 (2008).

- 
- [91] V. V. Mehta, M. Liberati, F. J. Wong, R. V. Chopdekar, E. Arenholz, and Y. Suzuki, *J. Appl. Phys.* **105**, 07E503 (2009).
- [92] A. D. Rata, A. Herklotz, L. Schultz, and K. Doerr, *EPJ B* **76**, 215 (2010).
- [93] J. W. Freeland, J. X. Ma, and J. Shi, *Appl. Phys. Lett.* **93**, 212501 (2008).
- [94] A. Herklotz, A. D. Rata, L. Schultz, and K. Doerr, *Phys. Rev. B* **79**, 092409 (2009).
- [95] H. Hsu, P. Blaha, and R. M. Wentzcovitch, *Phys. Rev. B* **85**, 140404 (2012).
- [96] M. Merz, P. Nagel, C. Pinta, A. Samartsev, H. v Loehneysen, M. Wissinger, S. Uebe, A. Assmann, D. Fuchs, and S. Schuppler, *Phys. Rev. B* **82**, 174416 (2010).
- [97] C. Pinta, D. Fuchs, M. Merz, M. Wissinger, E. Arac, H. Von Loehneysen, A. Samartsev, P. Nagel, and S. Schuppler, *Phys. Rev. B* **78**, 174402 (2008).
- [98] S. Murata, S. Isida, M. Suzuki, Y. Kobayashi, K. Asai, and K. Kohn, *Physica B* **263**, 647 (1999).
- [99] K. D. Kreuer, S. Adams, W. Munch, A. Fuchs, U. Klock, and J. Maier, *Solid State Ionics* **145**, 295 (2001).
- [100] L. Malavasi, C. A. J. Fisher, and M. S. Islam, *Chem. Soc. Rev.* **39**, 4370 (2010).
- [101] J.-R. Martinez, C. E. Mohn, S. Stoelen, and N. L. Allan, *J. Solid State Chem.* **180**, 3388 (2007).
- [102] F. Ramezanipour, J. E. Greedan, A. Grosvenor, J. F. Britten, L. M. D. Cranswick, and V. O. Garlea, *Chem. Mater.* **22**, 6008 (2010).
- [103] V. Jayaraman, A. Magrez, M. Caldes, O. Joubert, F. Taulelle, J. Rodriguez-Carvajal, Y. Piffard, and L. Brohan, *Solid State Ionics* **170**, 25 (2004).
- [104] K. D. Kreuer, T. Esaka, H. Uchida, and N. Maeda, *Anun. Rev. Matter.* **33**, 333 (2003).
- [105] M. S. Islam, P. F. Slater, and T. Tolchard, *J. R. and Dinges, Dalton Trans.* p. 3061 (2004).
- [106] W. Münch, G. Seifert, K. D. Kreuer, and J. Maier, *Solid State Ionics* **86**, 647 (1996).

- [107] J. Bednorz and K. Müller, Z. Phys. B **64**, 189 (1986).
- [108] M. Wu, J. Ashburn, C. Torng, P. Hor, R. Meng, L. Gao, Z. Huang, Y. Wang, and C. Chu, Phys. Rev. Lett. **58**, 908 (1987).
- [109] Y. Kamihara, T. Watanabe, M. Hirano, and H. Hosono, J. Am. Chem. Soc. **130**, 3296 (2008).
- [110] I. Mazin, Nature **464**, 183 (2010).
- [111] K. Oshida, Y. Nakai, and H. Hosono, J. Phys. Soc. Jpn. **78**, 062001 (2009).
- [112] A. Schilling, M. Cantoni, J. Guo, and H. Ott, Nature **363**, 56 (1993).
- [113] Z.-A. Ren, W. Lu, J. Yang, W. Yi, X.-L. Shen, Z.-C. Li, G.-C. Che, X.-L. Dong, L.-L. Sun, F. Zhou, and Z.-X. Zhao, Chin. Phys. Lett. **25**, 2215 (2008).
- [114] P. Quebe, L. Terbüchte, and W. Jeitschko, J. All. and Comp. **302**, 70 (2000).
- [115] J. Zhao, Q. Huang, C. Cruz, L. Shiliang, J. Lynn, Y. Chen, M. Green, G. Chen, G. Li, J. Luo, N. Wang, and P. Dai, Nature Materials **7**, 953 (2008).
- [116] C.-H. Lee, A. Iyo, H. Eisaki, H. Kito, M. Fernandez-Diaz, T. Ito, K. Kihou, H. Matsuhata, M. Braden, and K. Yamada, J. Phys. Soc. Jpn. **77**, 083704 (2008).
- [117] Z. Ren and Z. Zhao, Adv. Mater. **21**, 4584 (2009).
- [118] T. Ozawa and S. Kauzlarich, Sci. Technol. Adv. Mater. **9**, 03303 (2008).
- [119] M. Rotter, M. Tegel, and D. Johrendt, Phys. Rev. Lett. **101**, 107006 (2008).
- [120] X. Wang, Q. Liu, Y. Lv., W. Gao, L. Yang, R. Yu, F. Li, and C. Jin, Solid State Comm. **148**, 538 (2008).
- [121] Y. Mizuguchi, F. Tomioka, S. Tsuda, T. Yamaguchi, and Y. Takano, J. Phys. Soc. Jpn. **78**, 074712 (2009).
- [122] J. Bardeen, L. Cooper, and J. Schrieffer, Phys. Rev. **108**, 1175 (1957).
- [123] J. Waldram, *Superconductivity of metals and cuprates* (IOP Publishing, Bristol, 1996).
- [124] I. Mazin, D. Singh, M. Johannes, and M.H.Du, Phys. Rev. Lett. **101**, 057003 (2008).

- 
- [125] M. Tinkham, *Introduction to Superconductivity, 2nd ed* (Dover Publications, Mineola, 1996).
- [126] D. Harshman, J. Dow, and A. Fiory, *Phys. Rev. B* **77**, 024523 (2008).
- [127] R. Liu, T. Wu, G. Wu, G. Chen, X. Wang, Y. Xie, J. Ying, Y. Yan, Q. Li, B. Shi, W. Chu, Z. Wu, *et al.*, *Nature* **459**, 64 (2009).
- [128] C. Cruz, Q. Huang, J. Lynn, J. Li, W. Ratcliff, J. Zarestky, H. Mook, G. Chen, J. Luo, N. Wang, and P. Dai, *Nature* **453**, 899 (2008).
- [129] H.-H. Klauss, H. Luetkens, R. Klingeler, C. Hess, F. Litterst, M. Kraken, M. Korshunov, I. Eremin, S.-L. Drechsler, R. Khasanov, A. Amato, J. Hamann-Borrero, *et al.*, *Phys. Rev. Lett.* **101**, 077005 (2008).
- [130] J. Noffsinger, F. Giustino, S. Louie, and M. Cohen, *Phys. Rev. Lett.* **102**, 147003 (2009).
- [131] S. Jiang, C. Wang, Z. Ren, Y. Luo, G. Cao, and Z. Xu, *J. Phys. Cond. Mat.* **21**, 382203 (2009).
- [132] A. Sefat, R. Jin, M. McGuire, B. Sales, D. Singh, and D. Mandrus, *Phys. Rev. Lett.* **101**, 117004 (2008).
- [133] Z.-A. Ren, G.-C. Che, X.-L. Dong, J. Yang, W. Lu, W. Yi, X.-L. Shen, Z.-C. Li, L.-L. Sun, F. Zhou, and Z.-X. Zhao, *Euro Phys. Lett.* **83**, 17002 (2008).
- [134] H. Okada, K. Igawa, H. Takahashi, Y. Kamihara, M. Hirano, H. Hosono, K. Matsubayashi, and Y. Uwatoko, *J. Phys. Soc. Jpn.* **77**, 113712 (2008).
- [135] G. Xiao, F. Streitz, A. Gavrin, Y. Du, and C. Chien, *Phys. Rev. B* **35**, 8782 (1987).
- [136] D. Bonn, *Nature Physics* **2**, 153 (2006).
- [137] J. Dong, H. Zhang, G. Xu, Z. Li, G. Li, Z. Hu, D. Wu, G. Chen, X. Dai, J. Luo, Z. Fang, and N. Wang, *Euro. Phys. Lett.* **83**, 27006 (2008).
- [138] D. Singh, *Physica C* **469**, 418 (2009).
- [139] C. C. Tsuei, J. R. Kirtley, Z. F. Ren, J. H. Wang, H. Raffy, and Z. Z. Li, *Nature* **387**, 481 (1997).
- [140] T. Kondo, A. Santander-Syro, O. Copie, C. Liu, M. Tillman, E. Mun, J. Schmalian, S. Bud'ko, M. Tanatar, P. Canfield, and A. Kaminski, *Phys. Rev. Lett.* **101**, 147003 (2008).
- [141] A. Chubukov, I. Eremin, and M. Korshunov, *Phys. Rev. B* **79**, 220501(R) (2009).

- [142] M. Rahlenbeck, G. Sun, D. Sun, C. Lin, B. Keimer, and C. Ulrich, *Phys. Rev. B* **80**, 064509 (2009).
- [143] V. Hadijev, M. Iliev, K. Sasmal, Y.-Y. Sun, and C. Chu, *Phys. Rev. B* **77**, 220505 (2008).
- [144] L. Chauviere, Y. Gallais, M. Cazayous, A. Sacuto, and M. Measson, *Phys. Rev. B* **80**, 094594 (2009).
- [145] K. Choi, D. Wulferding, P. Lemmens, N. Ni, S. Budko, and P. Canfield, *Phys. Rev. B* **78**, 212503 (2008).
- [146] D. N. Basov, R. D. Averitt, D. van der Marel, M. Dressel, and K. Haule, *Rev. Mod. Phys.* **83**, 471 (2011).
- [147] C. Kuebler, H. Ehrke, R. Huber, R. Lopez, A. Halabica, R. F. Haglund, Jr., and A. Leitenstorfer, *Phys. Rev. Lett.* **99**, 116401 (2007).
- [148] A. Pashkin, C. Kübler, H. Ehrek, R. Lopez, A. Halabica, R. F. Haglund Jr., R. Huber, and A. Leitenstorfer, *Phys. Rev. B* **83**, 195120 (2011).
- [149] C. V. Shank, R. Yen, and C. Hirlimann, *Phys. Rev. Lett.* **50**, 454 (1983).
- [150] C. V. Shank, R. Yen, and C. Hirlimann, *Phys. Rev. Lett.* **51**, 900 (1983).
- [151] M. Schultze, E. M. Bothschafter, A. Sommer, S. Holzner, W. Schweinberger, M. Fiess, M. Hofstetter, R. Kienberger, V. Apalkov, V. S. Yakovlev, M. I. Stockman, and F. Krausz, *Nature*, *Advance online publication* (2012).
- [152] A. Schiffrin, T. Paasch-Colberg, N. Karpowicz, V. Apalkov, D. Gerster, S. Mühlbrandt, M. Korbman, J. Reichert, M. Shultze, S. Holzner, J. V. Barth, R. Kienberger, *et al.*, *Nature*, *Advance online publication* (2012).
- [153] S. Dal Conte, C. Giannetti, G. Coslovich, F. Cilento, D. Bossini, T. Abebaw, F. Banfi, G. Ferrini, H. Eisaki, M. Greven, A. Damascelli, D. van der Marel, *et al.*, *Science* **335**, 1600 (2012).
- [154] D. H. Torchinsky, J. W. McIver, D. Hsieh, G. F. Chen, J. L. Luo, N. L. Wang, and N. Gedik, *Phys. Rev. B* **84**, 104518 (2011).
- [155] F. Jenkins and H. White, *Fundamentals of optics, 4th ed.* (McGraw-Hill Book Company, New York, 1976).
- [156] C. Rulliere (Ed.), *Femtosecond Laser Pulses, Principles and Experiments* (Springer-Verlag, Berlin, 1998).

- 
- [157] J. Diels and W. Rudolph, *Ultrashort Laser Pulse Phenomena* (Academic Press, London, 2006).
- [158] E. Hecht, *Optics, 4th ed.* (Addison Wesley, San Francisco, 2002).
- [159] F. Pedrotti and L. Pedrotti, *Introduction to Optics, 2nd ed.* (Prentice Hall International Editions, London, 1993).
- [160] *Guide to streak cameras*, [http://sales.hamamatsu.com/assets/pdf/catsandguides/e\\_streakh.pdf](http://sales.hamamatsu.com/assets/pdf/catsandguides/e_streakh.pdf).
- [161] *TOPAS User's manual*.
- [162] R. Averitt and A. Taylor, *J. Phys.: Condens. Matter* **14**, R1357 (2002).
- [163] T. Ogasawara, K. Ohgushi, Y. Tomioka, K. Takahashi, H. Okamoto, M. Kawasaki, and Y. Tokura, *Phys. Rev. Lett.* **94**, 087202 (2005).
- [164] S. Sundaram and E. Mazur, *Nature Mater.* **1**, 217 (2002).
- [165] E. Beaurepaire, J.-C. Merle, A. Daunois, and J.-Y. Bigot, *Phys. Rev. Lett.* **76**, 4250 (1996).
- [166] C.-K. Sun, F. Vallée, L. H. Acioli, E. P. Ippen, and J. G. Fujimoto, *Phys. Rev. B* **50**, 15337 (1994).
- [167] A. Sabbah and D. Riffe, *Phys. Rev. B* **66**, 165217 (2002).
- [168] N. Del Fatti, C. Voisin, M. Achermann, S. Tzortzakis, D. Christofilos, and F. Vallée, *Phys. Rev. B* **61**, 16956 (2000).
- [169] R. H. M. Groenvelde, R. Sprik, and A. Lagendijk, *Phys. Rev. B* **51**, 11433 (1995).
- [170] F. Rossi and T. Kuhn, *Rev. Mod. Phys.* **74**, 895 (2002).
- [171] H. Okamoto, T. Miyagoe, K. Kobayashi, H. Uemura, H. Nishioka, H. Matsuzaki, A. Sawa, and Y. Tokura, *Phys. Rev. B* **83**, 125102 (2012).
- [172] C. V. Raman and K. S. Krishnan, *Nature* **121**, 501 (1928).
- [173] G. Landsberg and L. Mandelstam, *Naturwissenschaften* **16**, 57 (1928).
- [174] M. G. Cottam and D. J. Lockwood, *Light scattering in magnetic solids* (John Wiley and Sons, New York, 1986).
- [175] R. D. Mattuck, *A Guide to Feynman Diagrams in the Many-Body Problem* (Dover Publications, New York, 1992).

- 
- [176] A. Pinczuk and E. Burstein, *Topics in Applied Physics: Light Scattering in Solids I* (Springer-Verlag New York, 1983), chap. Fundamentals of Inelastic Light Scattering in Semiconductors and Insulators.
- [177] L. D. Landau and E. M. Lifshitz, *Statistical Physics, 3rd Edition part 1* (Butterworth-Heinemann, Oxford, 1980).
- [178] R. Kubo, *Adv. Chem. Phys.* **15**, 101 (1969).
- [179] J. R. Schmidt, N. Sundlass, and J. L. Skinner, *Chem. Phys. Lett.* **378**, 559 (2003).
- [180] P. G. Klemens, *Phys. Rev.* **148**, 845 (1966).
- [181] J. Menendez and M. Cardona, *Phys. Rev. B* **29**, 2051 (1983).
- [182] M. Calandra, M. Lazzeri, and F. Mauri, *Physica C* **456**, 38 (2007).
- [183] M. N. Iliev, M. V. Abrashev, V. N. Popov, and V. G. Hadijev, *Phys. Rev. B* **67**, 212301 (2003).
- [184] N. D. Todorov, M. V. Abrashev, and V. G. Ivanov, *J. Phys.: Condens. Matter* **24**, 175404 (2012).

